# Supplementary information for

## Identifying the components of the solid–electrolyte interphase in Li-ion Batteries

Luning Wang[1], Anjali Menakath[2], Fudong Han[3], Yi Wang[1], Peter Y. Zavalij[1], Karen Gaskell[1], Oleg Borodin[4], Dinu Iuga[2], Steven P. Brown[2], Chunsheng Wang[1,3*], Kang Xu[4*] and Bryan W. Eichhorn[1*]

*[1]Department of Chemistry and Biochemistry, University of Maryland, College Park, MD 20742, USA.*

*[2]Department of Physics, University of Warwick, Coventry, CV4 7AL, United Kingdom.*

*[3]Department of Chemical and Biomolecular Engineering, University of Maryland, College Park, MD 20742, USA*

*[4]Electrochemistry Branch, Power and Energy Division Sensor and Electron Devices Directorate, U.S. Army Research Laboratory, Adelphi, MD 20783, USA.*

# Contents


1. Experimental and Results ..... 3
  1.1 General regents and instruments ..... 3
  1.2 Chemical synthesis and characterizations ..... 4
    1.2.1 Lithium methyl carbonate (LMC). ..... 4
    1.2.2 Lithium ethylene mono-carbonate (LEMC) ..... 4
    1.2.3 Lithium ethylene di-carbonate·2 dimethyl sulfoxide (LEDC·2DMSO). ..... 4
    1.2.4 Amorphous LEDC. ..... 5
  1.3 Interconversion/equilibria studies ..... 5
    1.3.1 Studies of equilibria constants. ..... 5
    1.3.2 Synthesis of mono lithium ethylene glycolate ($LiOCH_2CH_2OH$) and lithium methoxide, MeOLi. 5
    1.3.3 Reactions of LEDC + DMC in DMSO ..... 6
    1.3.4 Reactions of LMC + LiEG in DMSO. ..... 6
    1.3.5 Reactions of LEDC + LiEG in DMSO ..... 6
    1.3.6 Reactions of LEMC + MeOLi in DMSO ..... 6
    1.3.7 Reactions of LEDC + EG in DMSO ..... 6
    1.3.8 Reactions of LEMC + DMC (No DMSO) ..... 6
    1.3.9 Reactions of LEDC + DMC (No DMSO) ..... 7
    1.3.10 Reactions of LEMC + 1M $LiPF_6$ in EC/DMC (No DMSO) ..... 7
    1.3.11 Reactions of LiOH + EC (No DMSO) ..... 7
    1.3.12 Reactions of MeOLi + EC (No DMSO) ..... 7
  1.4 Electrochemical measurements and SEI detection by solution NMR spectroscopy ..... 7
  1.5 Solid-state NMR analysis on chemical standards and graphite SEI layers ..... 8
    1.5.1 $^1H$ – $^1H$ Double Quantum (DQ) MAS[2] ..... 9
    1.5.2 $^7Li$ – $^1H$ Heteronuclear single quantum correlation (HMQC) experiments ..... 9
    1.5.3 Density functional theory (DFT) calculations on solid-state NMR spectra ..... 9
  1.6 Quantum chemistry calculations on LEMC/LEDC hydrolysis ..... 10
  1.7 Born Oppenheimer Molecular Dynamics Simulations of LEMC ..... 10
    1.7.1 Simulation results ..... 10
    1.7.2 Born-Oppenheimer Molecular Dynamics Simulation Methodology: ..... 11
2. Supplementary Figures ..... 13
3. Supplementary Tables ..... 46
4. References ..... 51

# 1. Experimental and Results

## 1.1 General regents and instruments

All air/moisture-sensitive chemical reagents were stored under inert atmosphere. Anhydrous ethylene carbonate (EC), Sure/Seal dimethyl carbonate (DMC), Sure/Seal ethylene glycol (EG), Sure/Seal 2.5 M n-BuLi/hexane, Sure/seal 1.6 M MeLi/diethyl ether, ethylene diamine and tetrahydrofuran (THF) were purchased from Sigma-Aldrich. Deuterium Oxide ($D_2O$, 99.9%) and dimethyl sulfoxide (DMSO-$d_6$, 99.9%) were purchased from Cambridge Isotope Laboratories Inc. Diethyl ether, N-Methyl-2-pyrrolidone (NMP), dimethyl formamide (DMF), tert-butyl alcohol, pyridine and anhydrous AcroSeal methanol (MeOH) were obtained from Fisher Scientific. DMSO, Lithium (Li) foil, Potassium (K) metal cube, Tin (Sn) powder and $LiPF_6$ were purchased from Alfa Aesar. $CO_2$ tank was purchased from Airgas. Graphite (TIMCAL TIMREX KS44) and polyvinylidene fluoride (PVDF) were purchased from commercial sources.
Nuclear Magnetic Resonance (NMR) spectra were recorded at 25 $^oC$ on a Bruker 400 MHz, Bruker DRX-500 MHz, Bruker AVIII-600 MHz or Bruker Ascend-800 MHz high resolution spectrometers. All NMR spectra collected in DMSO-$d_6$ were referenced to DMSO-$d_6$ at 2.500 ppm for $^1H$ NMR, 39.52 ppm for $^{13}C\{^1H\}$ NMR, or 1M LiCl in $D_2O$ at 0 ppm for $^7Li$ NMR. NMR spectra collected in $D_2O$ were referenced to EC at 4.500 ppm. Chemical shifts (δ) were reported in ppm and multiplicities were indicated by s (singlet), d (doublet), t (triplet), q (quartet), m (multiplet), br (broad). Coupling constants *J* were reported in Hertz (Hz). Powder X-ray diffraction (XRD) patterns were collected on a Bruker C2 Discover spectrometer with a 2D detector, or on a Bruker D8 spectrometer. Single-crystal XRD data were recorded on a Bruker Apex2 diffractometer equipped with Apex2 CCD area detector, graphite monochromator and mono cap collimator. Fourier transform infrared spectroscopy (FTIR) was carried out employing a Thermo Nicolet 670 spectrometer in a diffuse reflectance (DRIFTS) cell. Electrochemical tests of batteries were carried out either in a beaker or a swagelock-type cell in an Ar-filled glovebox with a Pine Wavenow USB potentiostat. Elemental analysis on C, H and N were performed by combustion method by Midwest Microlab. Elemental analysis on Li were performed by a ICPE-9000 inductively coupled plasma (ICP) atomic emission spectrometer (AES). X-ray photoelectron spectroscopy (XPS) measurements were carried out on a high sensitivity Kratos AXIS 165 spectrometer with an Al anode for X-ray source. All the XPS spectra were calibrated to the adventitious hydrocarbon (AdvHC) carbon at 284.8 eV.

Strict protocols were followed to certify all reagents were moisture-free. Prior to use, DMSO, DMF and pyridine were distilled over $CaH_2$. DMSO-$d_6$ and DMC were dried over activated 4A molecular sieves (prior to use, the molecular sieves were activated at 400 $^oC$ under vacuum for over 12 h). Diethyl ether and THF were distilled from Na benzophenone. Ethylene diamine was distilled from $K_4Sn_9$. $LiPF_6$ was dried under vacuum in a Schlenk line for 12 h at 50 $^oC$. All graphite electrodes were dried in a vacuum oven at 100 $^oC$ for at least 5 h. $CO_2$ was dried by passing through a $CaSO_4$ column.

The minimal level of moisture in DMSO-$d_6$ used for NMR analysis was further certified by $K_4Sn_9$/ethylene diamine solution. Synthesis of $K_4Sn_9$ was reported elsewhere.[1] *ca.* 10 mg $K_4Sn_9$ were dissolved in 10 ml anhydrous ethylene diamine to form a dark red solution. An aliquot (*ca*. 5 mg) of the solution was added to *ca.* 0.5 ml DMSO-$d_6$, upon which the colorless DMSO turned red. The minimal level of moisture in the DMSO-$d_6$ solution was certified if the red color in the $K_4Sn_9$/ethylene diamine/DMSO-$d_6$ solution was able to persist while no precipitate observed for at least 12 h. $^1H$ NMR spectroscopy measurements were extensively applied to ensure all liquid reagents/electrolytes had no contamination.

## 1.2 Chemical synthesis and characterizations

Unless otherwise noted, all reactions were performed in oven-dried glassware with magnetic stirring under inert atmosphere in a Schlenk line or in an Ar-filled glovebox.

### *1.2.1 Lithium methyl carbonate (LMC).*

Elemental analysis. Calcd for $C_2H_3O_3Li$: C, 29.30; H, 3.69; N, 0. Found: C, 29.24; H, 3.81; N, 0.

NMR data collected on an NMR 500 MHz spectrometer at 25 °C in DMSO-$d_6$. 0.55 mol/L. (Supplementary Fig. 2)

$^1$H NMR (500 MHz, DMSO-$d_6$), δ 3.296 (s).

$^{13}$C {$^1$H NMR (126 MHz, DMSO-$d_6$), δ 157.38, 51.67.

$^7$Li NMR (194 MHz, DMSO-$d_6$) δ -0.689. (in reference to 1M LiCl in $D_2O$ at 0 ppm).

*Alert level B in CheckCif report:*

*Alert 1*. The minimum difference density is < -0.1*ZMAX*1.00

*Alert 2*. Large reported Min. (Negative) Residual Density -1.25 eA-3

*Response*: Due to substantial disorder of every other molecule, residual difference density is slightly larger.

### *1.2.2 Lithium ethylene mono-carbonate (LEMC)*

Elemental analysis. Calcd for $C_3H_5O_4Li$: C, 32.17; H, 4.50; N, 0; Li, 6.20. Found: C, 32.18; H, 4.50; N, 0; Li, 6.20.

NMR data collected on an NMR 500 MHz spectrometer at 25 °C in DMSO-$d_6$. 0.53 mol/L. (Supplementary Fig. 3)

$^1$H NMR (500 MHz, DMSO-$d_6$) δ 4.816 (br), 3.764 (s), 3.723 (t, $J$ = 5.4 Hz), 3.443 (t, $J$ = 5.5 Hz), 3.378 (s).

$^{13}$C {$^1$H} NMR (126 MHz, DMSO-$d_6$) δ 156.88, 156.61, 65.75, 63.30, 62.92, 60.99.

$^7$Li NMR (194 MHz, DMSO-$d_6$) δ 1.426. (in reference to 1M LiCl in $D_2O$ at 0 ppm).

*Alert level B in CheckCif report*:

Large Reported Max. (Positive) Residual Density 0.91 eA-3

*Response*: Slightly larger than expected residual difference density is due to presence of very minor impurities on the crystal as manual separation of single crystal from colorless grown-in agglomerates was quite complicated.

### *1.2.3 Lithium ethylene di-carbonate·2 dimethyl sulfoxide (LEDC·2DMSO).*

Elemental analysis. Calcd for $C_8H_{16}O_8S_2Li_2$: C, 30.19; H, 5.07; N, 0. Found: C, 30.37; H, 4.37; N, 0. (Deviation from theorical value is due to loss of lattice DMSO during sample analysis).

NMR data collected on an NMR 500 MHz spectrometer at 25 °C in DMSO. *ca.* 0.02 mol/L. (Supplementary Fig. 5)

$^{1}$H NMR (500 MHz, DMSO-$d_6$) δ 3.629 (s), 2.539 (s).

$^{13}$C {$^{1}$H} NMR (126 MHz, DMSO-$d_6$) δ 155.20, 62.73, 40.43.

$^{7}$Li NMR (194 MHz, DMSO-$d_6$) δ -1.084. (in reference to 1M LiCl in $D_2O$ at 0 ppm).

Synthesis of lithium tert-butoxide. To a Schlenk flask charged with a stirred solution of tert-butyl alcohol (4.0 g, 54 mmol) dissolved in anhydrous diethyl ether (20 ml) at 0 °C was added 2.5 M n-BuLi/hexane (21.6 ml, 54 mmol, 1 equiv.) dropwise. The reaction was allowed to warm to room temperature and further stirred for 30 min. Afterwards diethyl ether was removed under vacuum, generating a white powder of lithium tert-butoxide (3.85 g, 88% yield).

#### *1.2.4 Amorphous LEDC.*

The as-synthesized LEDC·2DMSO (268 mg) was suspended in anhydrous THF (20 ml). The suspension solution was sonicated at 50 °C for 3 h under an inert atmosphere. The solid powder in the suspension was collected by centrifugation, rinsed with anhydrous THF and vacuum dried for at least 24 h. The process leads to an amorphous powder of LEDC with some minor DMSO and THF residues. White powder, 105 mg. (powder XRD analysis in Supplementary Fig. 1 d, $^{1}$H NMR analysis in Supplementary Fig. 13)

### 1.3 Interconversion/equilibria studies

Unless otherwise noted, all reactions were performed under inert gas atmosphere in a Schlenk line or in an Ar-filled glovebox.

#### *1.3.1 Studies of equilibria constants.*

The equilibrium constant of chemical equilibrium 2 LEMC = LEDC + EG was studied via adding different amounts of EG into 5 solutions of LEMC dissolved in DMSO-$d_6$ solutions. Anhydrous acetonitrile (0.185 mol/L) was added into each solution as internal standard. Concentrations of the relevant chemical species in the 5 solutions were calculated against the peak areas in $^{1}$H NMR spectra.

The equilibria constant of chemical equilibrium LMC + EG = LEMC + MeOH was studied via adding different amounts of EG (0.151 – 1.210 equiv.) into 5 solutions of LMC (initial concentration: 0.343 mol/L) dissolved in DMSO-$d_6$ solutions. Anhydrous acetonitrile (0.161 mol/L) was added into each solution as internal standards. Concentrations of the relevant chemical species in the 5 solutions were calculated against the peak areas in $^{1}$H NMR spectra.

#### *1.3.2 Synthesis of mono lithium ethylene glycolate ($LiOCH_2CH_2OH$) and lithium methoxide, MeOLi.*

To a Schlenk flask charged with a stirred solution of EG (2.2 g, 35 mmol) dissolved in anhydrous diethyl ether (20 ml) at 0 °C was added 2.5 M n-BuLi/hexane (14 ml, 35 mmol, 1 equiv.) dropwise. White precipitate was observed immediately after the addition of n-BuLi. The reaction was allowed to warm to

room temperature and further stirred for 30 min. Afterwards diethyl ether was removed under vacuum, generating a white powder of LiEG ($LiOCH_2CH_2OH$). The powder was rinsed with anhydrous diethyl ether, dried under vacuum for over 12 h. (2.0 g, 85 % yield).

To a Schlenk flask charged with a stir bar and clean Li metal cubes (0.32 g, 45 mmol) at 0 °C was added anhydrous methanol (30 ml) dropwise. Bubbles were observed immediately. After all Li metal disappeared, the reaction was allowed to warm to room temperature and further reacted for 30 min. Methanol was removed by vacuum and a white powder of MeOLi was obtained. (1.61 g, 94% yield).

### *1.3.3 Reactions of LEDC + DMC in DMSO*

To a stirred solution of LEDC·2DMSO (7 mg) dissolved in DMSO-$d_6$ (0.7 g) was added excess DMC (19 mg). A clear solution was obtained and allowed to stir for 1 h, after which $^1$H NMR analysis were performed on the solution. (Supplementary Fig. 17 a).

### *1.3.4 Reactions of LMC + LiEG in DMSO.*

To a stirred solution of LMC (10 mg) dissolved in DMSO-$d_6$ (1g) was added LiEG (10 mg). LiEG did not dissolve and a suspension was obtained. The suspension was allowed to stir for 1 h, after which the supernatant was collected through centrifugation for $^1$H NMR analysis. (Supplementary Fig. 17 b).

### *1.3.5 Reactions of LEDC + LiEG in DMSO*

To a stirred solution of LEDC·2DMSO (10 mg) dissolved in DMSO-$d_6$ (1.1 g) was added LiEG (7 mg). LiEG did not dissolve and a suspension was obtained. The suspension was allowed to stir for 1 h, after which the supernatant was collected through centrifugation for $^1$H NMR analysis. (Supplementary Fig. 17 c).

### *1.3.6 Reactions of LEMC + MeOLi in DMSO*

To a stirred solution of LEMC (20 mg) dissolved in DMSO-$d_6$ (1g) was added MeOLi (11 mg). MeOLi did not dissolve and a suspension was obtained. The suspension was allowed to stir for 1 h, after which the supernatant was collected through centrifugation for $^1$H NMR analysis. (Supplementary Fig. 17 d).

### *1.3.7 Reactions of LEDC + EG in DMSO*

To a stirred solution of LEDC·2DMSO (7 mg) dissolved in DMSO-$d_6$ (0.75 g) was added EG (2 mg). A clear solution was obtained and allowed to stir for 10 min, after which $^1$H NMR analysis were performed on the solution. (Supplementary Fig. 18).

### *1.3.8 Reactions of LEMC + DMC (No DMSO)*

To 5 ml vials charged with 1g 1M $LiPF_6$/DMC solutions was added LEMC (20 mg). LEMC did not dissolve and the powder/solution mixtures were allowed to sit for different amount of time (2 days to 5 weeks),

after which the precipitate was collected through centrifugation. As any residual DMC in the precipitate would incur secondary reactions with remaining LEMC after dissolved in DMSO-$d_6$, the obtained precipitate was rinsed thoroughly with anhydrous acetonitrile 5 times, dried under vacuum for 2 h to remove residual DMC, and dissolved in DMSO-$d_6$ for $^1$H NMR analysis. (Supplementary Fig. 26 a).

#### *1.3.9 Reactions of LEDC + DMC (No DMSO)*

To 5 ml vials charged with 1g 1M $LiPF_6$/DMC solutions was added LEDC·2DMSO (40 mg). LEDC·2DMSO did not dissolve and the powder/solution mixtures were allowed to sit for different amounts of time (up to 4 weeks), after which the precipitates were collected through centrifugation. The obtained precipitate was rinsed thoroughly with anhydrous acetonitrile 5 times, dried under vacuum for 2 h to remove residual DMC, and dissolved in DMSO-$d_6$ for $^1$H NMR analysis. (Supplementary Fig. 26 b).

#### *1.3.10 Reactions of LEMC + 1M $LiPF_6$ in EC/DMC (No DMSO)*

To 5 ml vials charged with 1g 1M $LiPF_6$ EC/DMC solutions was added LEMC (20 mg). LEMC did not dissolve and the powder/solution mixtures were allowed to sit (no stirring) for different amounts of time (up to 6 weeks), after which the precipitates were collected through centrifugation. The obtained precipitate was rinsed thoroughly with anhydrous acetonitrile 5 times, dried under vacuum for 2 h to remove residual DMC, and dissolved in DMSO-$d_6$ for $^1$H NMR analysis. (Supplementary Fig. 26 c).

#### *1.3.11 Reactions of LiOH + EC (No DMSO)*

Anhydrous LiOH (100 mg) was reacted with 2 g 1M $LiPF_6$/EC, 1M $LiPF_6$/DMC or 1M $LiPF_6$/EC/DMC at room temperature under fast stirring in an Ar-filled glovebox for 24 h. The reaction precipitates and supernatants were separated by centrifugation. The precipitates in the three reactions were collected, rinsed with anhydrous acetonitrile thoroughly, vacuum dried (30 min) and extracted into DMSO-$d_6$ for $^1$H NMR analysis (Supplementary Fig. 33).

#### *1.3.12 Reactions of MeOLi + EC (No DMSO)*

LiOMe (50 mg) was reacted with EC (10 g) under stirring in an Ar atmosphere at 50 $^o$C for 48 h. Afterwards, the reaction mixture was brought into an Ar-filled glovebox and turned to be a solid after cooled to room temperature. The solid mixture was rinsed thoroughly by anhydrous acetonitrile to remove soluble components (*e.g.*, EC), vacuum dried (30 min) and extracted into DMSO-$d_6$ for NMR analysis (Supplementary Fig. 34).

### 1.4 Electrochemical measurements and SEI detection by solution NMR spectroscopy

All graphite electrodes were fabricated in the air without carbon black. Typically, a large electrode for detection of SEI layer components contained at least 400 mg graphite powder (Timex KS44). The

graphite powder was mixed with PVDF (by mass, graphite: PVDF = 10: 1) in an appropriate amount of NMP solvent (*ca*. 2 ml) to form a slurry, which was cast onto a Cu current collector (*ca*. 200 $cm^2$) to make a graphite electrode. Graphite electrodes cut into diameter of ½ inch were also fabricated in a similar method. All electrodes were dried in an 80 °C oven overnight, followed by in a 100 °C vacuum for at least 5 h, transferred instantly into an Ar-filled glovebox.

All electrochemical tests and SEI layer extractions were performed in an Ar-filled glovebox unless otherwise noted. Electrochemical tests were performed either in a beaker for the large graphite electrode, or in a swagelock-type cell for the ½ inch electrode. Three types of electrolytes were used, namely 1M $LiPF_6$ in DMC, 1M $LiPF_6$ in EC/DMC (v: v = 1: 1) and 1 M $LiPF_6$ in EC (mixing 1.52 g $LiPF_6$ and 13 g EC forms a liquid solution at 27 °C).

After the large graphite electrodes were cycled for three times from 0.7 V – 2.0 V, the electrodes were recovered from the electrolyte solution in their charged state. Graphite electrodes cycled in electrolytes of EC/DMC, or DMC-only were rinsed by anhydrous DMC, while the graphite electrode cycled in the EC-only cell was rinsed by anhydrous acetonitrile. All electrodes were further vacuum dried for at least 12 h to remove volatile solvent, immersed into 2 ml DMSO-$d_6$ for 3 h or 2 ml 0.1 M DCl/$D_2O$ solution for 10 min to extract SEI layer components. 1D and 2D NMR spectra were recorded on the DMSO-$d_6$ and $D_2O$ solutions employing a 500 MHz, 600 MHz or 800 MHz NMR spectrometer.

**NMR data in DMSO-$d_6$. (25 °C)**

(Fig. 6 a) $^1$H NMR (800 MHz, DMSO-$d_6$) δ 5.059 (t, *J* = 5.1 Hz), 4.480 (s), 4.294 (s), 4.092 (q, *J* = 5.3 Hz), 3.895 (d, *J* = 10.0 Hz), 3.706 (s), 3.693 (s), 3.649 (s), 3.430 – 3.410 (m), 3.391 – 3.381 (m), 3.215 (s), 3.167 (d, *J* = 5.4 Hz).

(Fig. 6 c) $^{13}$C {$^1$H} NMR (201 MHz, DMSO-$d_6$) δ 155.88, 155.83, 155.72, 155.53, 154.95, 65.39, 65.31, 64.99, 62.79, 61.92, 54.80, 54.66, 51.00, 48.59.

(Fig. 6 d) $^1$H NMR (500 MHz, DMSO-$d_6$) δ 3.731 (t, *J* = 5.4 Hz), 3.457 (q, *J* = 5.4 Hz), 3.402 – 3.393 (m).

**NMR data in 0.1 M DCl/$D_2O$. (25 °C)**

(Fig. 6 b) $^1$H NMR (500 MHz, $D_2O$) δ 4.704 (s), 4.500 (s), 4.302 (s), 3.687 (s), 3.668 (s), 3.548 (s), 3.235 (s), 2.608 (s).

## 1.5 Solid-state NMR analysis on chemical standards and graphite SEI layers

After a large graphite electrode cast on Cu current collector was cycled from 0.7 – 2.0 V *vs.* Li foil in an electrolyte solution of 1M $LiPF_6$ in EC/DMC (v: v = 1: 1) for 3 times, the electrode was recovered at its charged state, rinsed with anhydrous DMC and vacuumed to remove volatile solvents. Afterwards, the SEI-coated graphite powder was carefully scraped off of the Cu current collector with a blade in an inert atmosphere. The SEI-coated graphite powder, along with chemical standards (LMC, LEMC and LEDC·2DMSO) were all packed in a glovebox under nitrogen atmosphere to reduce the amount of exposure of the samples to air and moisture.

All solid-state NMR experiments were recorded on a Bruker Avance III HD 850 spectrometer operating at a Larmor frequency of 850.2 MHz for $^1$H and 330.4 MHz for $^7$Li using a 1.3 mm triple resonance probe operating in double resonance mode at a MAS frequency of 60 kHz (unless specified). A $^1$H 90° pulse

duration of 1.5 μs and a recycle delay of 3 s was used in all experiments. The $^{7}$Li pulse duration was 2.5 μs for a nutation frequency of 100 kHz.

### *1.5.1 $^{1}$H – $^{1}$H Double Quantum (DQ) MAS[2]*

Excitation and reconversion of DQ coherence were achieved using one rotor period of the BaBa (Back to Back) recoupling sequence.[3,4] A 16-step nested phase cycle was used to select $\Delta p = \pm 2$ during excitation and $\Delta p = -1$ on the z-filter 90° pulse, where $p$ is the coherence order. 16 transients were co-added for each of 160 (for LMC and LEDC.2DMSO) or 128 (for LEMC) $t_1$ FIDs, using the States – TPPI method to achieve sign discrimination in $F_1$ with a rotor synchronized $t_1$ increment of 16.67 μs, corresponding to a total experimental time of 1 h 9 mins (for LMC and LEDC.2DMSO) or 1 h 26 mins (for LEMC). See Supplementary Fig. 7 for the spectra.

### *1.5.2 $^{7}$Li – $^{1}$H Heteronuclear single quantum correlation (HMQC) experiments*

A $^{7}$Li -$^{1}$H HMQC pulse sequence utilizing rotary resonance recoupling ($R^3$),[5] which applies an $^{1}$H RF nutation frequency equal to twice the spinning frequency, that is a modified version of the pulse sequence of Gan et.al[6] was used. A second $^{1}$H 90° pulse (90° out of phase with respect to that of the first 90°) was applied shortly after a first $^{1}$H 90° pulse, while a phase inversion (every rotor period) of the $R^3$ pulses was used.[7,8] 16 transients were co-added for each of 128 $t_1$ FIDS, using states – TPPI method with a rotor synchronized $t_1$ increment of 16.67 μs corresponding to a maximum $t_1$ delay of 1.1 ms (Note that the $^{7}$Li FID is thus truncated in comparison to the case for the 1D spectra which were recorded with 20 ms acquisition time, hence explaining the observed broader linewidths in the 2D spectra). A $R^3$ recoupling time of 400 μs was used to observe one bond Li-H correlations. See Supplementary Fig. 7 for the spectra.

In all experiments, $^{1}$H chemical shifts are referenced using adamantane (higher ppm $^{1}$H resonance, 1.85 ppm) corresponding to TMS at 0 ppm[9] and $^{7}$Li is referenced to Lithium chloride at 8 ppm.[10,11]

### *1.5.3 Density functional theory (DFT) calculations on solid-state NMR spectra*

Calculations were performed for the crystal structure of LEMC and LMC using the Castep code[12,13] (academic release version 16.1), which implements DFT within a generalized gradient approximation. The crystal structures were geometry optimized by keeping the unit cell dimensions fixed. NMR shielding calculations were carried out using the GIPAW (gauge-including projector augmented wave)[14] method to find out the shielding tensor for each nucleus in the crystal structure. Both geometry optimization and NMR shielding calculations used a plane wave basis set and the PBE exchange correlation functional[15] using a ultrasoft pseudopotential,[16] with a maximum cut-off energy of 700 eV, with a minimum Monkhorst-pack grid[17] spacing of 2π × 0.1 Å$^{-1}$. To compare the results with experimentally measured isotropic chemical shifts directly, the below equation is used:

$$\delta_{iso} = \sigma_{ref} - \sigma_{iso} .$$

$\sigma_{ref}$ values for $^{1}$H, $^{13}$C, $^{7}$Li were 30.0, 170.0 and 90.9 ppm, respectively, as obtained by plotting the experimental chemical shift against the absolute the GIPAW calculated absolute shielding (by fixing

slope to -1).[18,19] The GIPAW calculated NMR shieldings are viewed and tabulated through the Magres view,[20] a visualization tool developed by CCP-NC (the collaborative computational project for NMR crystallography , www.ccpnc.ac.uk). Comparisons between simulated and collected data are presented in Supplementary Fig. 6, Supplementary Table 4 and 5.

## 1.6 Quantum chemistry calculations on LEMC/LEDC hydrolysis

Hydrolysis of LEMC and LEDC is investigated using quantum chemistry (QC) calculations. Gaussian g16 Gaussian software (revision b)[21] is used for all calculations. A polarized continuum model PCM with dielectric constant e=20 is used to implicitely include solvent in QC calculations. Reaction energies are calculated using the forth generation composite methodology G4MP2 unless specified otherwise.[22,23] G4MP2 is chosen for calculations because it was shown to accurately predict enthalpies of formation of neutral molecules, atomization energies, ionization potentials, electron affinities, proton affinities, and hydrogen bond energies.[23]

Screening of multiple reactant configurations yielded two low energy configurations shown in Supplementary Fig. 25 as R1 and R2 for LEMC + $Li^+(H_2O)$ and R3 and R4 for LEDC + $Li^+(H_2O)$. Hydrolysis of LEMC and LEDC is slightly endergonic relative to the most stable reactant configurations R2 and R4, but becomes exergonic relative to reactants R1 and R3 in agreement with experimental data**.** In order to examince the dependensce of reaction energies on the QC methodology, reaction energies for the LEMC hydrolysis were also calculated using coupled cluster with single, double and triple excitations CCSD(T) methodology with aug-cc-pvTz basis set. Geometries from MP2/aug-cc-pvTz calculations are used for calculating CCSD(T)/aug-cc-pvTz energy. Hydrolysis energy from R2 state of LEMC+$Li^+(H_2O)$ to LiEG + $Li^+HCO_3$ is 11.2 kJ/mol from CCSD(T)/aug-cc-pvTz calcuations for in close agreement G4MP2 free energy of 11.8 kJ/mol. Good agreement between these methods indicates reliability of G4MP2 predictions. We conclude that QC calculations indicate that hydrolysis of LEMC and LEDC is likely and is somewhat dependent on the water binding motif.

## 1.7 Born Oppenheimer Molecular Dynamics Simulations of LEMC

### *1.7.1 Simulation results*

The lithium transport mechanism is determined by the concentration of charge carriers and their diffusion coefficients.[24,25] The concentration of charge carries depends on the electrochemical potential the material is exposed to, the vacancy formation energies in bulk and at interfaces with electrolytes or other SEI compounds. Due to complications with the calculations of defect formation energies due to multiple OH group reorientations in LEMC, we first examined the $Li^+$ transport mechanism in LEMC. Two related solid state electrolytes (SSE) have been recently studied using DFT: a) the $Li_2CO_3$ crystal, [24,25] that also contains carbonate groups with the $Li^+$ cations packed between the layers of $CO_3^-$ anions instead of the alkyl carbonate $HO(CH_2)OCO_2^-$ anions; and b) the $Li_2OHCl$ SSE that is relevant to LEMC because of the presence of the OH groups located near the $Li^+$ cations and were shown to enhance the $Li^+$ transport through the revolving door mechanism.[26-28] We investigated if the $Li^+$ transport mechanism in LEMC is similar to that in $Li_2CO3$ or $Li_2OHCl$, or is somewhere in between after we verified that at 0K, DFT calculations yielded LEMC cell parameters of 12.58 Å, 5.31 Å and 13.91 Å in good agreement with the cell parameters of 12.66 Å., 5.20 Å., 14.09 Å from X-ray diffraction.

In $Li_2OHCl$ SSE, high concentration of the rotating OH-groups resulted in the fast $Li^+$ transport without introduction of any additional defects. In order to examine if the same revolving door mechanism is present in LEMC, Born Oppenheimer molecular dynamics (BOMD) simulations were performed on LEMC crystal using dispersion corrected Perdew–Burke-Ernzerhof (PBE-Grimme's D3) functional. A periodic simulation supercell (1x3x1) comprised of 24 LEMC was used in all DFT simulations with simulation details given below. First, we simulated the overheated LEMC crystals at 700 K for 28 ps using the optimized structure at 0 K as the initial configuration after 5 ps temperature ramp-up to 700 K. No $Li^+$ jumps or long range diffusion were observed. Temperature of BOMD simulations was increased to 800 K and simulations were performed for 15 ps without any signs of the long range $Li^+$ diffusion. Temperature was further increased to 1000 K and 23.5 ps BOMD simulations were performed. Again, no $Li^+$ long range diffusion or well identified jumps were observed in contrast to the facile $Li^+$ diffusion in $Li_2OHCl$ in the same temperature range. We conclude that the absence of $Li^+$ transport in LEMC is due to significantly smaller concentration of the rotating OH-groups compared to $Li_2OHCl$, thus, defects are important in order to realize the long range $Li^+$ diffusion in LEMC.

Following previous DFT calculations on $Li_2CO_3$,[24,25] we examined in BOMD simulations the $Li^+$ transport as a result of the $Li^+$ cation vacancy ($V_{Li+}$), an excess $Li^+$ interstitial ($Li_i^+$) and the $H^+$ vacancy ($V_{H+}$). BOMD simulations of LEMC with $V_{Li+}$ showed fast diffusion with 5 $Li^+$ jumps occurring over 24.9 ps at 700 K as shown in Supplementary Fig. 15. Further examination of the jump events indicated that jumps were sequential and did not occur in a highly correlated fashion as observed in the fastest SSE.[29]

Shorter (8ps) BOMD simulations of LEMC with $Li_i^+$ showed that the excess $Li^+$ gets pushed into the anion layer as shown in Supplementary Fig. 16(a-b). During BOMD simulations the interstitial $Li^+$ returns from the anion layer to the $Li^+$ layer (as shown in blue in Supplementary Fig. 16(a-b)), it pushes another $Li^+$ shown in yellow that and knocks-off another $Li^+$ (shown in green) into the anion layer. This mechanism is similar to the knock-off mechanism proposed for the Li+ conduction in $Li_2CO_3$. [24,25] However, at 800 K, the $Li_i^+$ diffusion is found to be slower than diffusion via the $V_{Li+}$ mechanism at 700 K.

Near lithiated graphite anode, SEI is exposed to the highly reductive environment, which likely leads to $H_2$ evolution and $H^+$ defect formation in the interfacial layer near graphite. BOMD simulations of the LEMC crystal with one $H^+$ defect were performed at 800 ps. No $Li^+$ jumps or long range $Li^+$ diffusion was observed over 12 ps, indicating that $V_{Li}$ defects are not as effective as $V_{Li+}$ in facilitating the $Li^+$ transport. This result is in accord with a slower $Li^+$ transport in $Li_{3-x}OH_xCl$, where $Li^+$ transport decreased with decreasing fraction of rotating OH-groups and adding more negative O* with stronger Coulomb attraction to $Li^+$.[28] We conclude that initial BOMD simulations of the superheated LEMC showed the fastest transport when $V_{Li+}$ defects present mechanism yields the fastest diffusion.

When 4 $H^+$ from the O-H groups were substituted with $Li^+$ (*i.e.*, di-lithiated ethylene mono-carbonate, DLEMC), fast $Li^+$ diffusion was observed at 800 K with the diffusion coefficient of 2.3 x $10^{-10}$ $m^2/s$ in 15 ps BOMD simulations. This $Li^+$ diffusion coefficient is slightly slower than the $Li^+$ cation diffusion coefficient found in $Li_2OHCl$ but is faster than the $Li^+$ diffusion coefficient found in BOMD simulations of the $Li_{2.5}OH_{0.5}Cl$ overheated SSEs. This is a likely mechanism for the fast $Li^+$ conduction in LEMC near the anode surface that is expected to have high fraction of H substituted with $Li^+$ due to limited stability of O-H groups in the heavily reductive environment.

### *1.7.2 Born-Oppenheimer Molecular Dynamics Simulation Methodology:*

We closely followed previous BOMD simulation methodology used for $Li_2OHCl$ electrolytes.[28] It is briefly repeated here for convenience. QUICKSTEP module of the cpk2 code is used for BOMD simulations using the dual Gaussian and Plane Waves (GPW) method.[30,31] Valence electrons are described by an atom-

centered Gaussian double-zeta basis set augmented with a set of d-type or p-type polarization functions (DZVP-MOLOPT-SR-GTH) with core electrons described by norm-conserving Goedecker-Teter-Hutter (GTH) pseudopotentials with 3, 6, 7, and 1 valence electrons for Li, O, Cl, and H, respectively.[32,33] The gamma point supercell approach was used in combination with 3-dimensioanl Periodic Boundary Conditions (PBC). Calculations were performed using the spin-polarized Perdew-Burke-Ernzerhof (PBE) exchange correlation functional with Grimme's D3 dispersion correction.[34,35] The SCF energy convergence was set to $10^{-6}$ atomic units.[36] The auxiliary planewave basis energy cutoff was 600 Ry and the relative cutoff. The MD simulation settings consist of the NPT-isotropic ensemble employing a CSVR thermostat with a 50-fs time constant.[37] The external pressure was set to 1 bar with a barostat time constant of 500-fs. The nuclei are propagated by the velocity Verlet algorithm during MD simulations with a time step of 0.5-fs. A deuterium mass was used for all hydrogen atoms.

## 2. Supplementary Figures

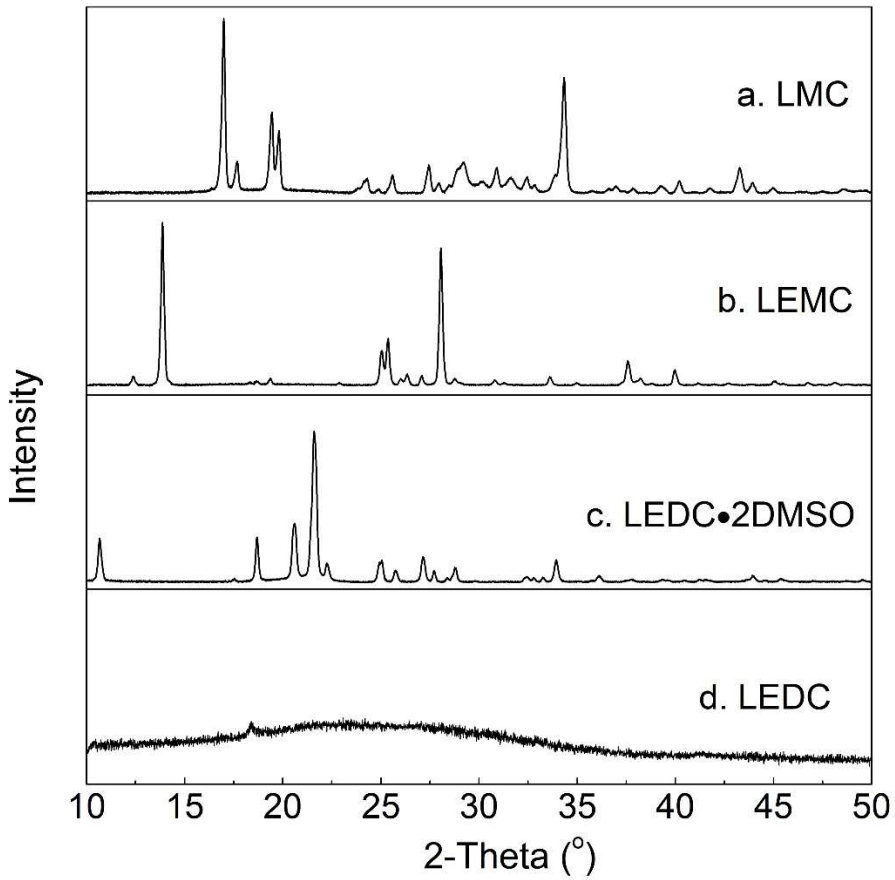


**Supplementary Figure 1**. Powder XRD data collected on (a) LMC, (b) LEMC, (c) LEDC·2DMSO and (d) amorphous LEDC obtained after DMSO solvates were removed from crystalline LEDC·2DMSO. Samples (a) (b) and (c) (d) were collected on Bruker D8 and Bruker C2 Discover spectrometers, respectively.

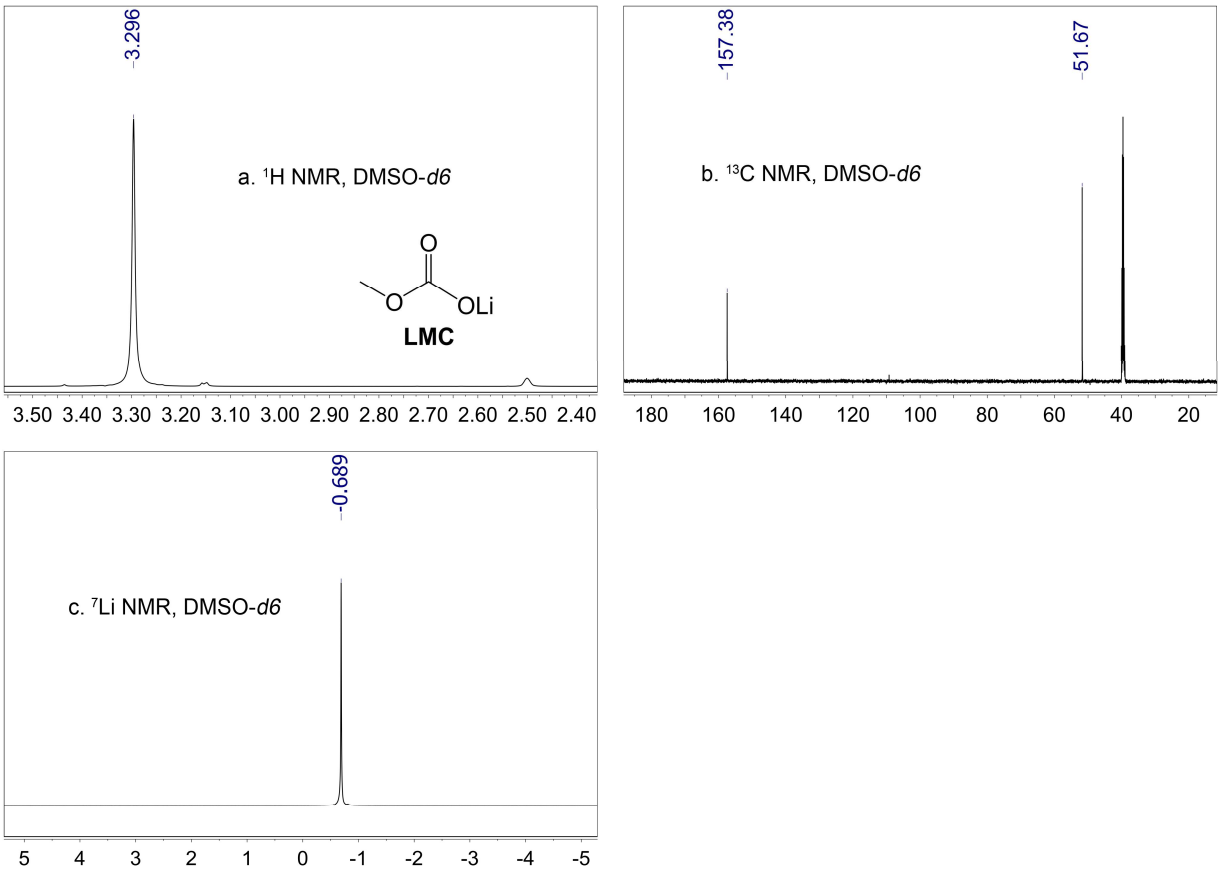


**Supplementary Figure 2.** (a) $^{1}$H NMR, (b) $^{13}$C {$^{1}$H} NMR and (c) $^{7}$Li NMR spectra of LMC in DMSO-$d_6$ (500 MHz, 0.55 mol/L, 25 $^{o}$C).

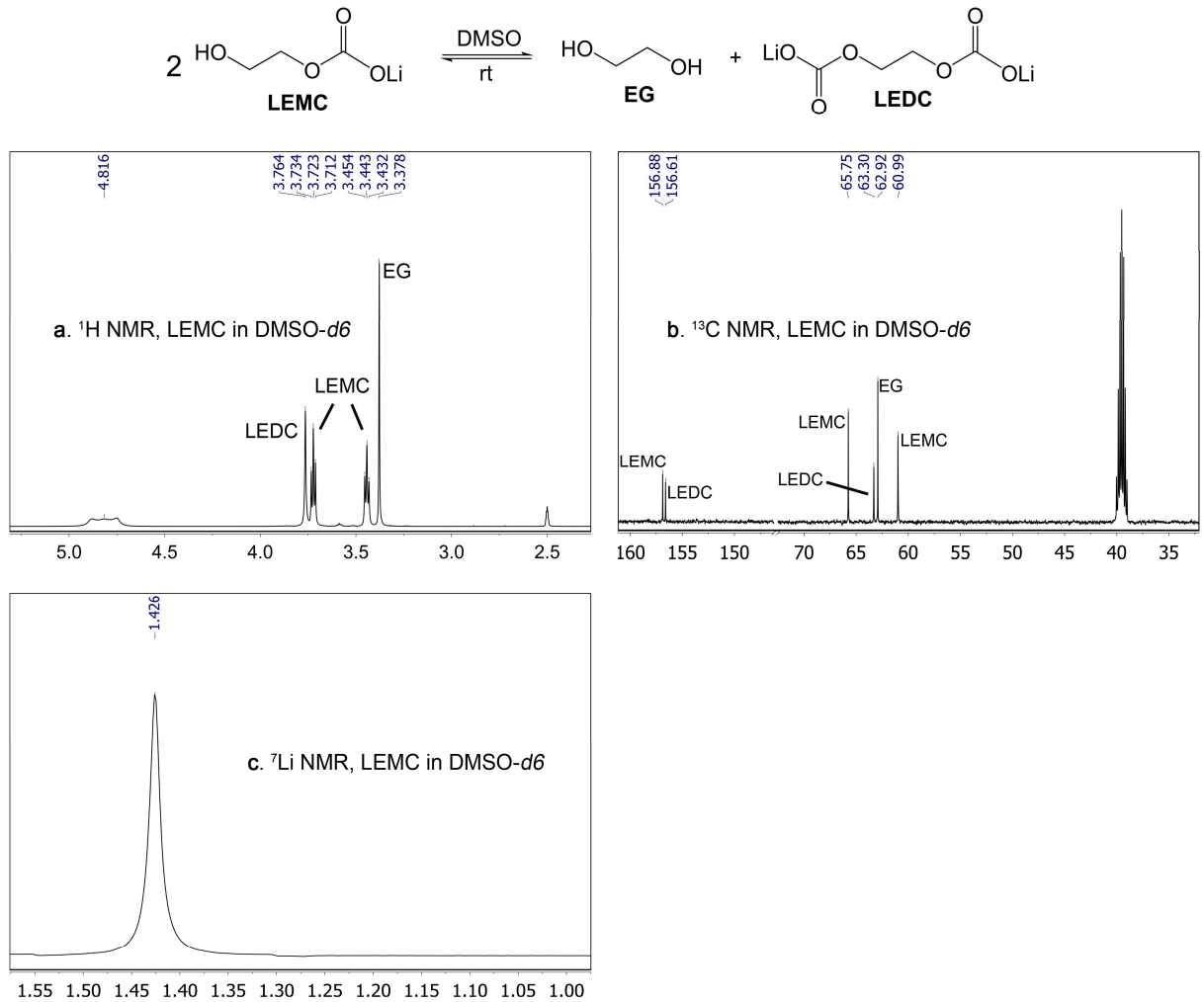


**Supplementary Figure 3**. (a) $^{1}$H NMR, (b) $^{13}$C {$^{1}$H} NMR and (c) $^{7}$Li NMR spectra of LEMC in DMSO-$d_6$ (500 MHz, 25 °C, 0.53 mol/L). Dissolving LEMC in the DMSO-$d_6$ solution generates LEDC and EG.

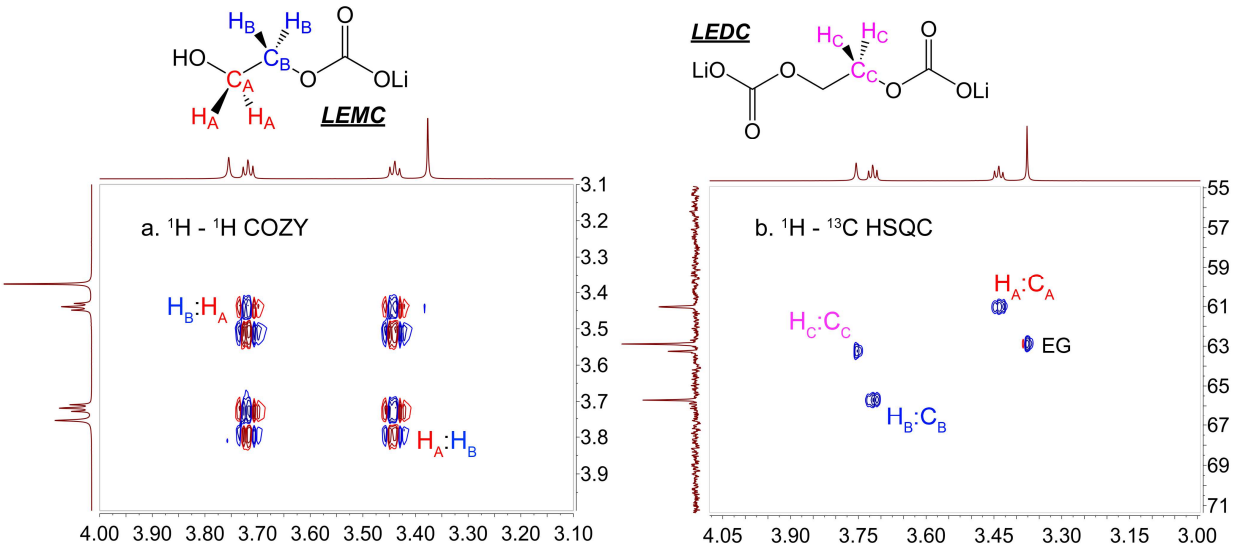


**Supplementary Figure 4**. (a) $^{1}$H-$^{1}$H correlated (COZY) and (b) $^{1}$H-$^{13}$C heteronuclear single quantum coherence (HSQC) spectra of LEMC dissolved in anhydrous DMSO-$d_6$ (600 MHz, 0.5 mol/L, 25 $^{o}$C). Dissolving LEMC in the DMSO-$d_6$ solution generates LEDC and EG.

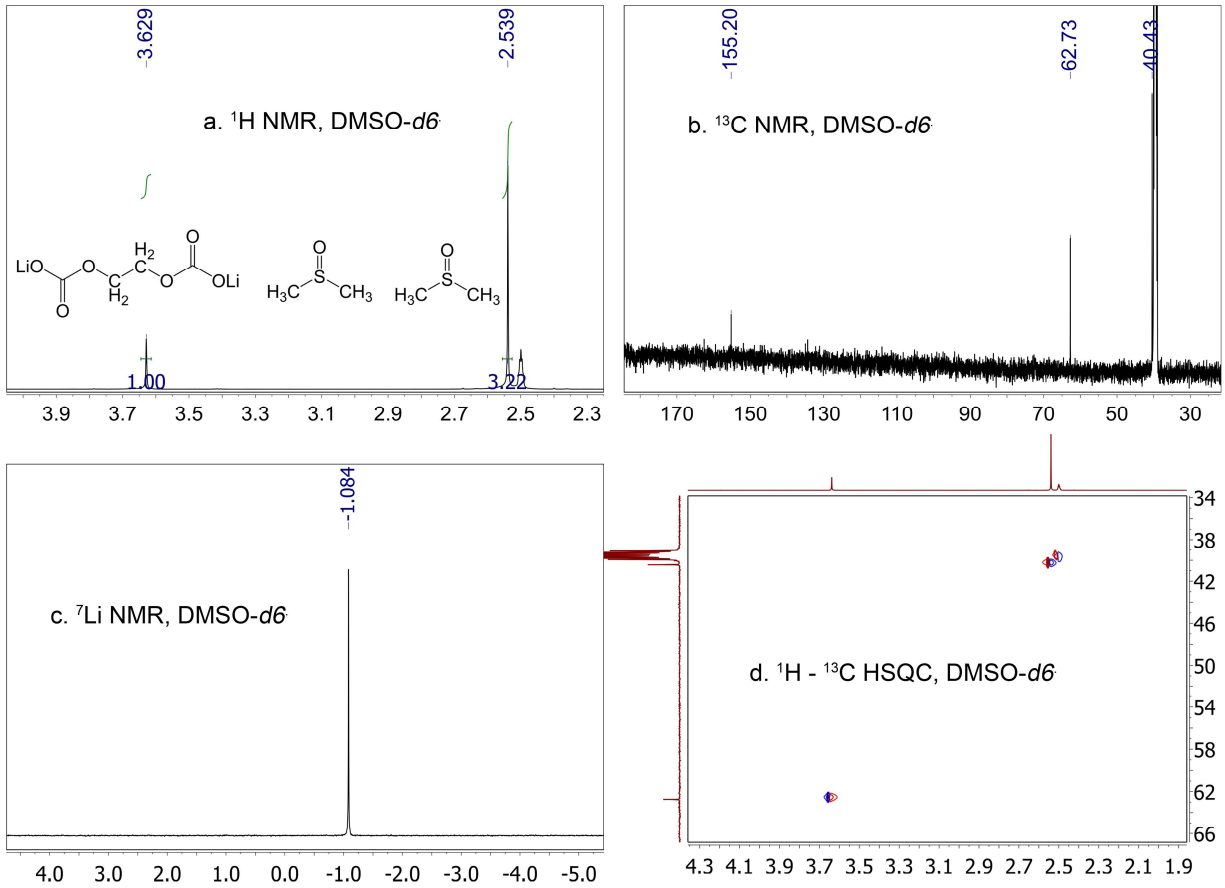


**Supplementary Figure 5**. (a) $^{1}$H NMR, (b) $^{13}$C {$^{1}$H} NMR, (c) $^{7}$Li NMR and (d) 2D $^{1}$H-$^{13}$C HSQC spectra of LEDC·2DMSO in DMSO-$d_6$ (*ca*. 0.02 mol/L). (a), (b) and (c) were recorded on an NMR 500 MHz spectrometer at 25 °C while (d) on an NMR 600 MHz spectrometer at 25 °C. Our experiment indicates much lower solubility of LEDC in DMSO-$d_6$ compared with LEMC and LMC.

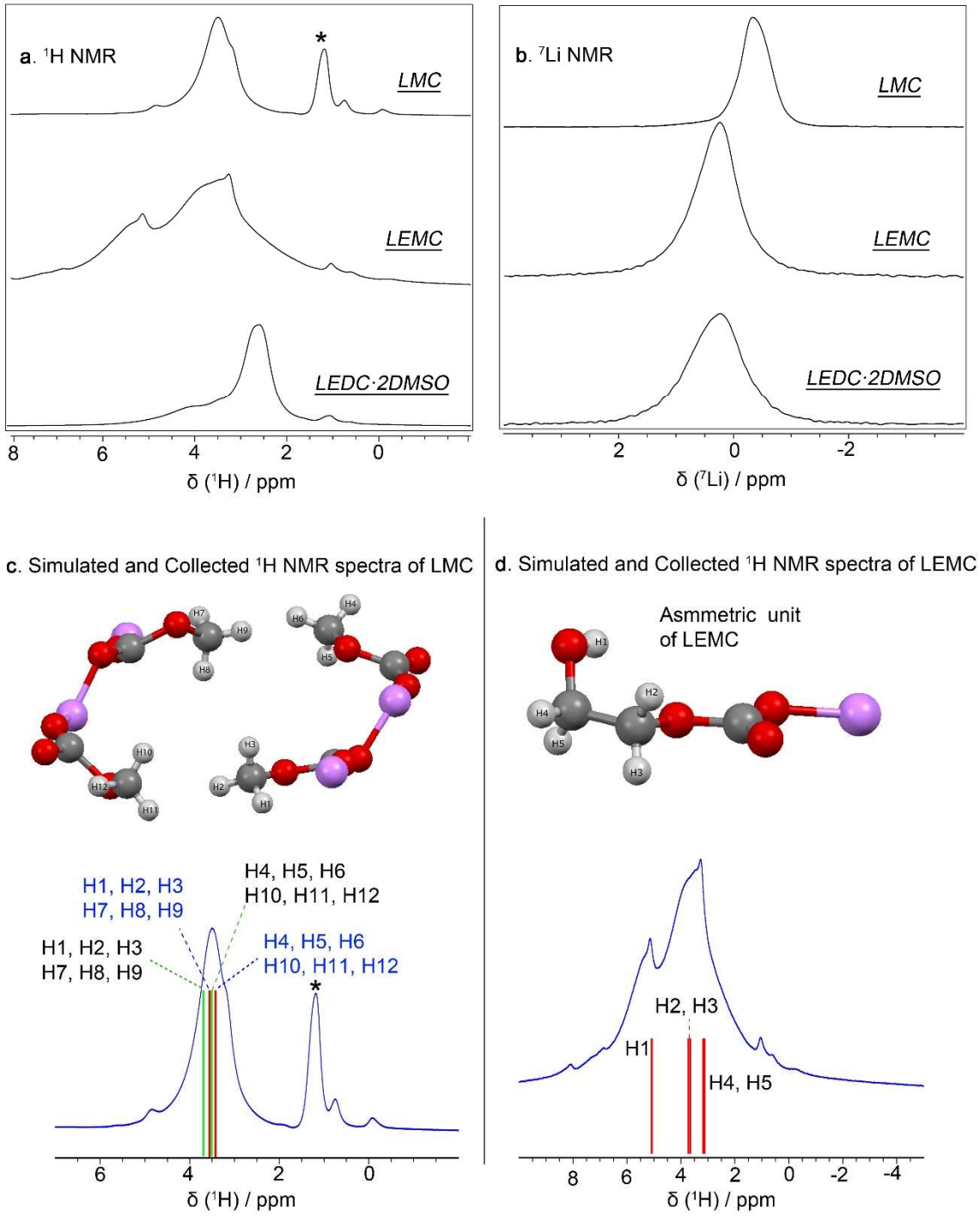


**Supplementary Figure 6.** 1D solid state NMR spectra. (a) $^{1}$H (850 MHz) and (b) $^{7}$Li (330 MHz) one pulse MAS NMR spectra of LMC, LEMC and LEDC·2DMSO. (c) LMC and (d) LEMC $^{1}$H (850 MHz) MAS (60 kHz) NMR spectra, together with the stick spectra corresponding to the GIPAW calculated chemical shifts for the geometry optimized (CASTEP) crystal structure models. * impurity (hydrolysis) due to sample preparation.

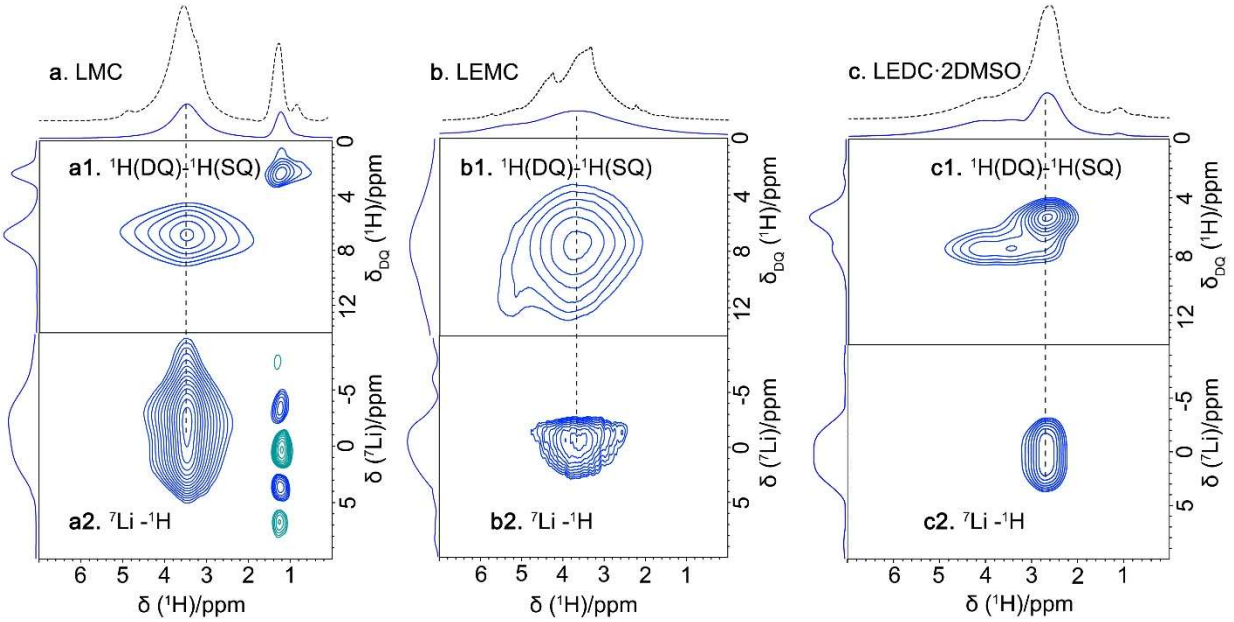


**Supplementary Figure 7.** (a1, b1 and c1) 2D $^{1}$H (850 MHz) (DQ)-$^{1}$H (SQ) MAS (60 kHz, with 1 $\tau_R$ of BABA recoupling), and (a2, b2 and c2) 2D $^{7}$Li-$^{1}$H (850 MHz) HMQC MAS (60 kHz, $\tau_{RCPL}$= 400 µs) NMR spectra of (a) LMC, (b) LEMC and (c) LEDC·2DMSO. For the 2D spectra, skyline projections are presented; in addition, at the top a 1D one-pulse $^{1}$H MAS NMR spectrum (dashed) is presented. The base contour levels are at 4 % and 14 % of the maximum peak intensity in (a1) and (a2) for LMC, 38 % and 44 % in (b1) and (b2) for LEMC, 22% and 20% for (c1) and (c2) for LEDC·2DMSO, respectively.

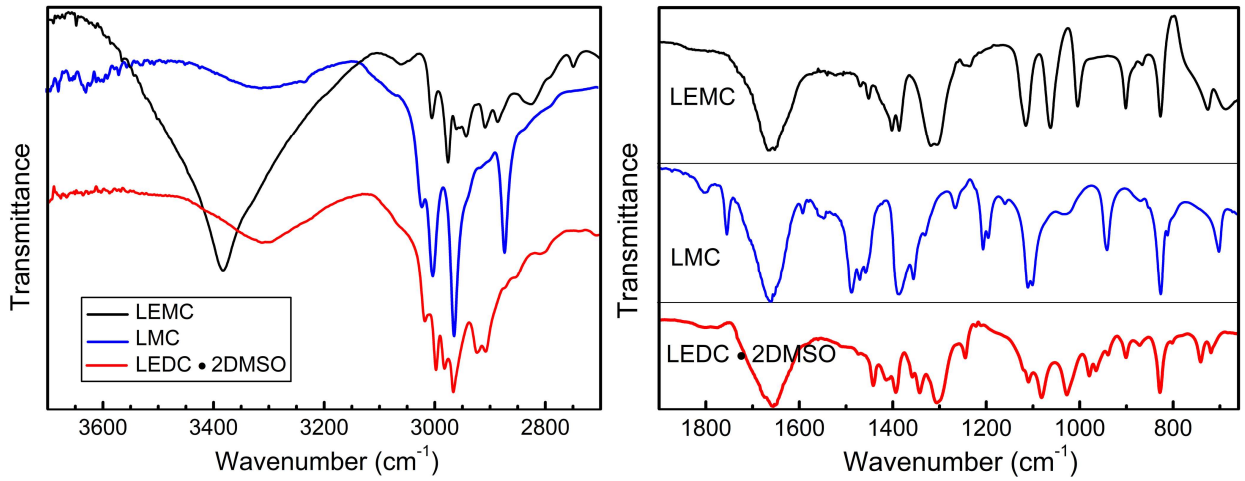


**Supplementary Figure 8**. FTIR spectra of LEMC (black), LMC (blue) and LEDC·2DMSO (red). LEMC shows a wide whereas sharp peak at 3380 $cm^{-1}$, in support of the presence of O-H hydrogen bonding in its crystalline lattice. Detailed assignment of the IR peaks is listed in Supplementary Table 1.

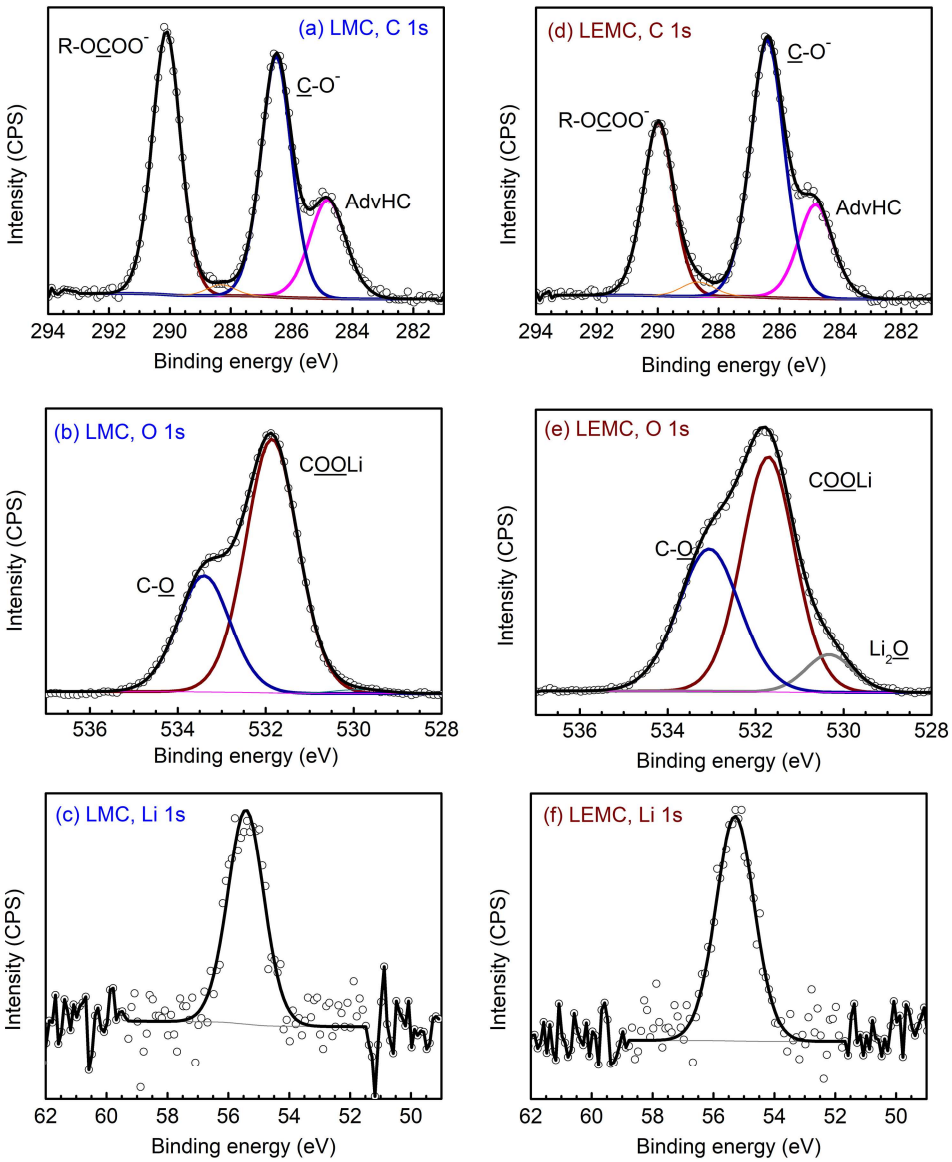


**Supplementary Figure 9.** XPS spectra of (a-c) LMC and (d-f) LEMC. All spectra are calibrated to adventitious hydrocarbon (AdvHC) at 284.8 eV.

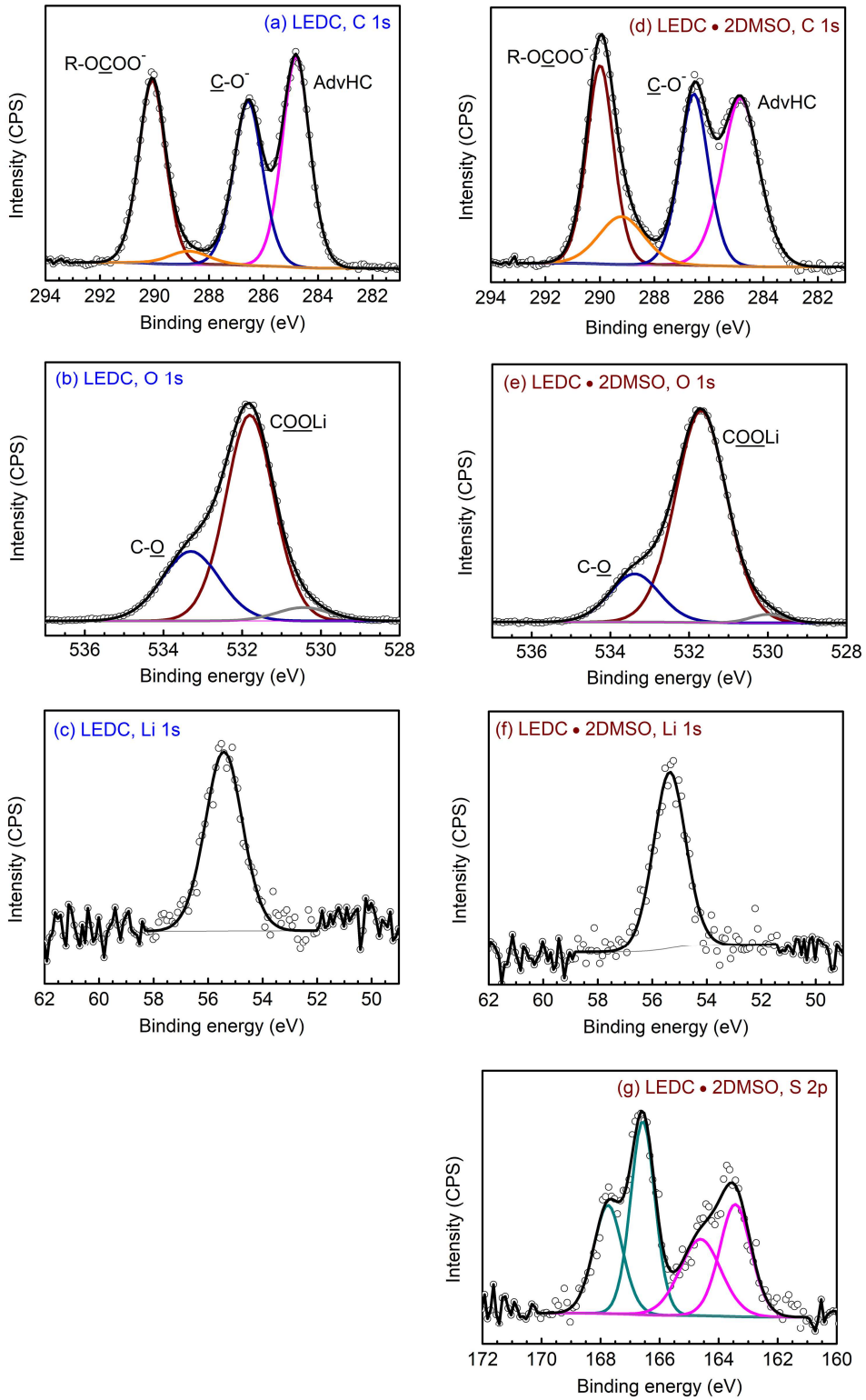


**Supplementary Figure 10.** XPS spectra of (a-c) amorphous LEDC and (d-g) LEDC·2DMSO. All spectra are calibrated to adventitious hydrocarbon (AdvHC) at 284.8 eV.

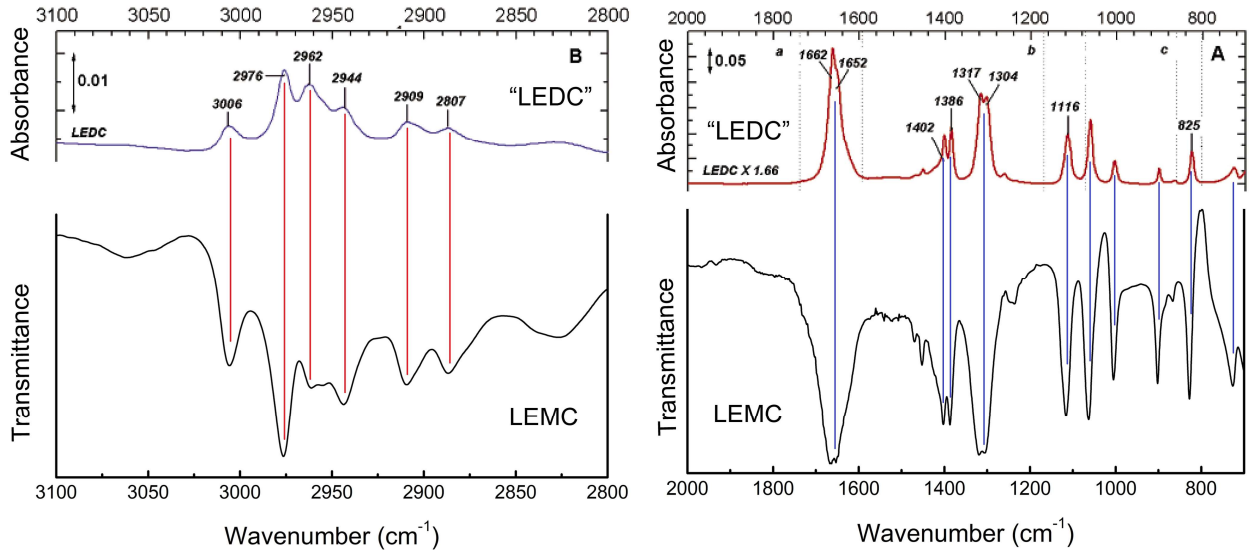


**Supplementary Figure 11.** Comparison of FTIR spectra of previously reported "LEDC"[38] and the LEMC of this work. Highly similar FTIR bands were observed. Reprinted with permission from ref. 38. Copyright 2006 American Chemical Society.

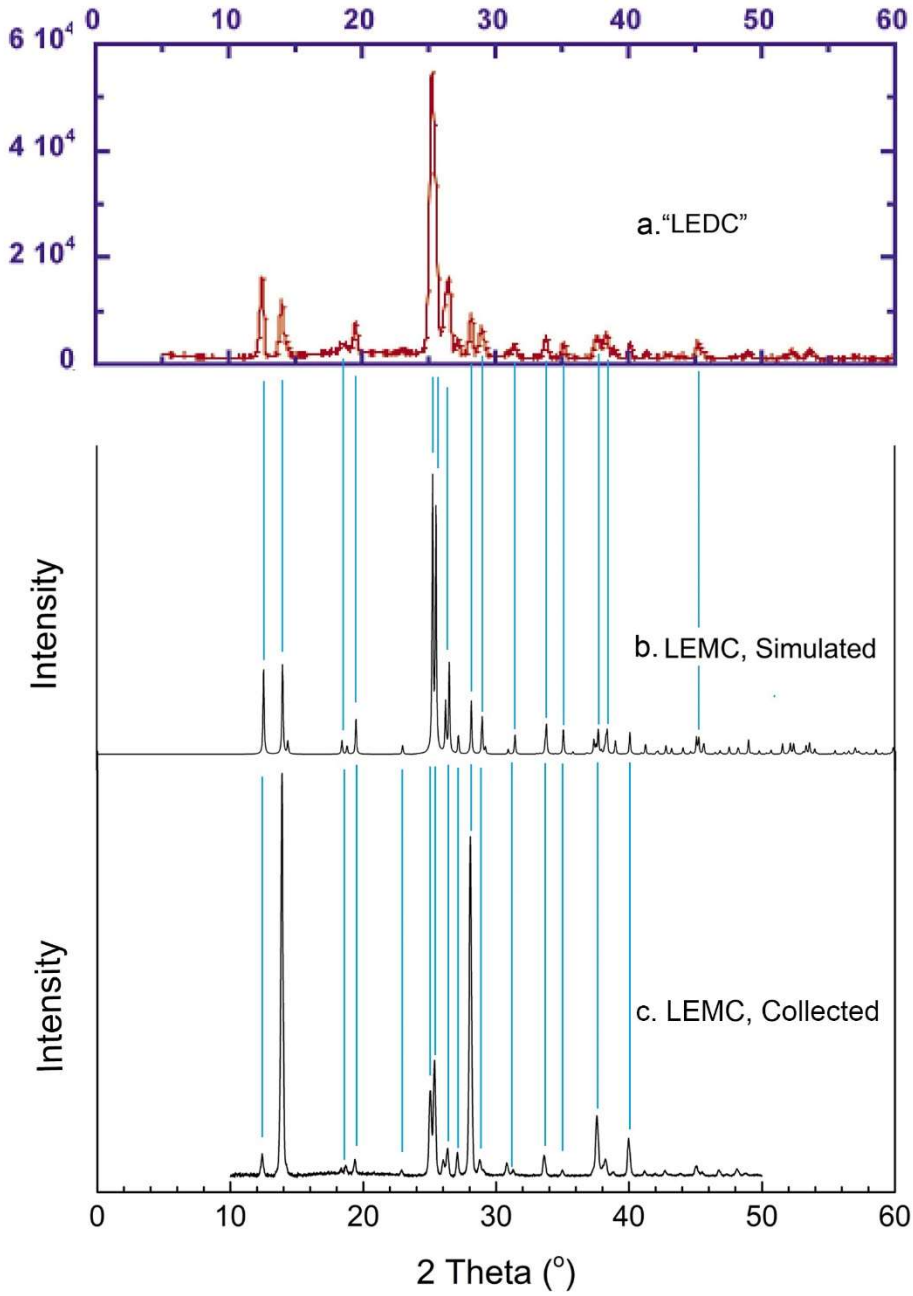


**Supplementary Figure 12.** Comparison of (a) previously reported XRD patterns on "LEDC",[38] (b) simulated XRD patterns from single crystalline structure of LEMC and (c) collected XRD patterns on LEMC of this work. Highly similar patterns were observed. The cell parameters of LEMC reported in this work (orthorhombic, a = 12.663 (3) Å, b = 5.1966 (10) Å, c = 14.091 (3) Å) are also in high similarity with the previously reported data of indexed powder XRD patterns (orthorhombic, a = 14.100 Å, b = 12.66 Å, c = 5.20 Å)[24]. Spectra in (c) were recorded on a Bruker D8 spectrometer on LEMC. Reprinted with permission from ref. 38. Copyright 2006 American Chemical Society.

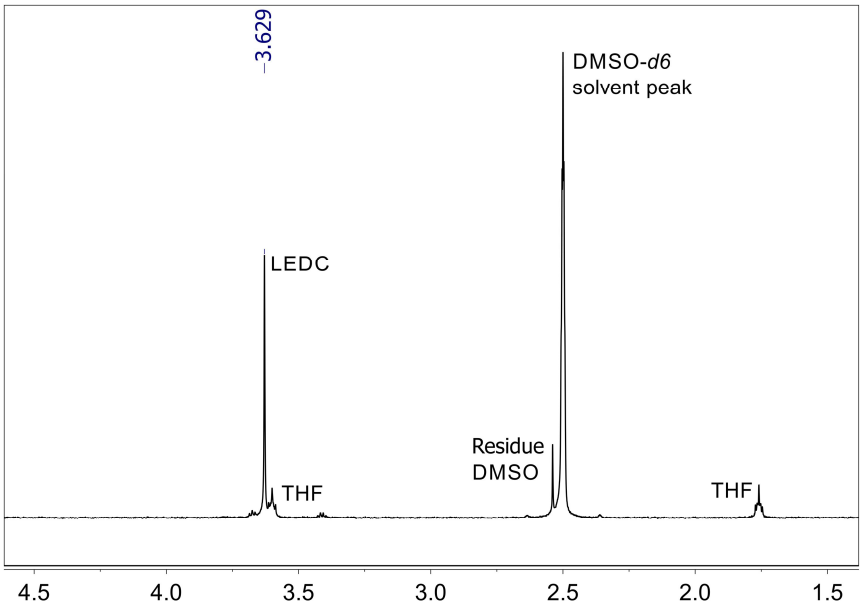


**Supplementary Figure 13.** $^{1}$H NMR spectra of the amorphous LEDC dissolved in DMSO-$d_6$ (500 MHz, *ca.* 0.02 mol/L, 25 °C). Residual DMSO and THF were observed.

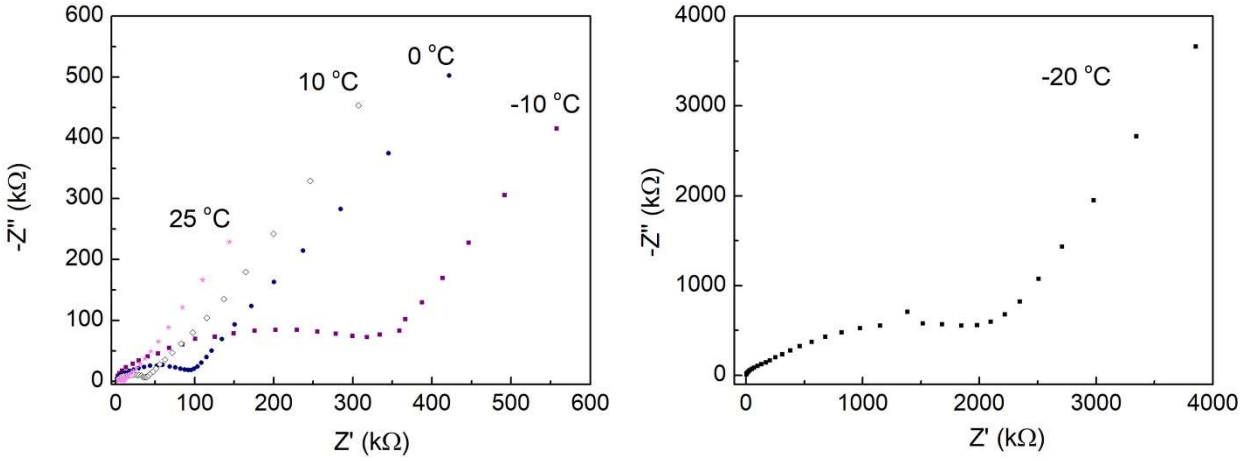


**Supplementary Figure 14.** EIS measurements on LEMC conducted under different temperatures.

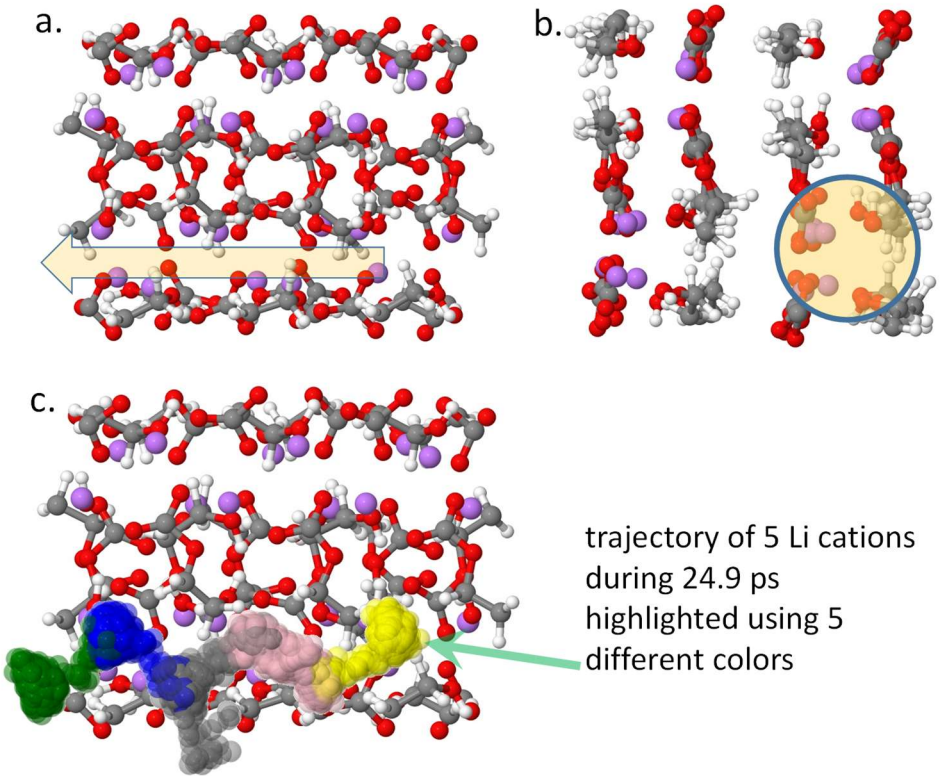


**Supplementary Figure 15.** Snapshots of the LEMC BOMD simulations with the direction of the $Li^+$ cation motion shown in (a) that is confined to the channel shown in (b), while the trajectory for the five fastest $Li^+$ cations is shown in (c) using three different colors (yellow, pink, grey, blue and green). Colors of the other atoms: H:white, Li: violet, C: grey, O: red.

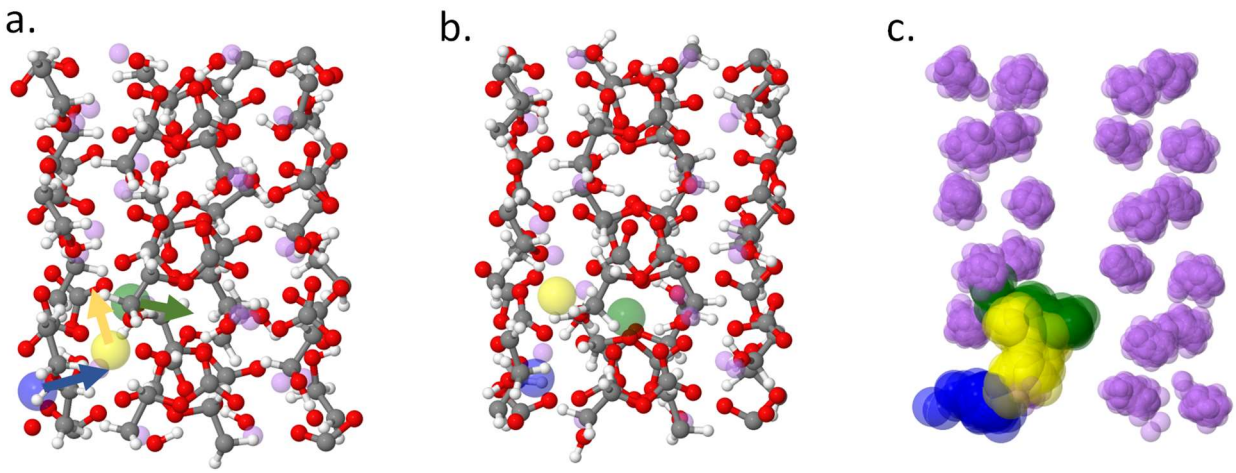


**Supplementary Figure 16.** Snapshots of LEMC solid-state electrolyte with one excess $Li^+$ cation from BOMD simulations at 800 K after 1 ps (a) and 5.5 ps (b). Thee $Li^+$ cations are enlarged in (a-c) and shown in blue, yellow and green, while all other $Li^+$ are shown in violet color. A tendency of the excess $Li^+$ to be knocked to the anion layer is highlighted in (a-b) using blue and green colored enlarged $Li^+$, respectively. Positions of all $Li^+$ superimposed on each other during 4.5 ps BOMD trajectory is shown in (c) with three most active $Li^+$ shown in blue, yellow and green, while the other $Li^+$ are shown as smaller violet balls. Colors of atoms in (a-b): H: white, Li: violet, C: grey, O: red.

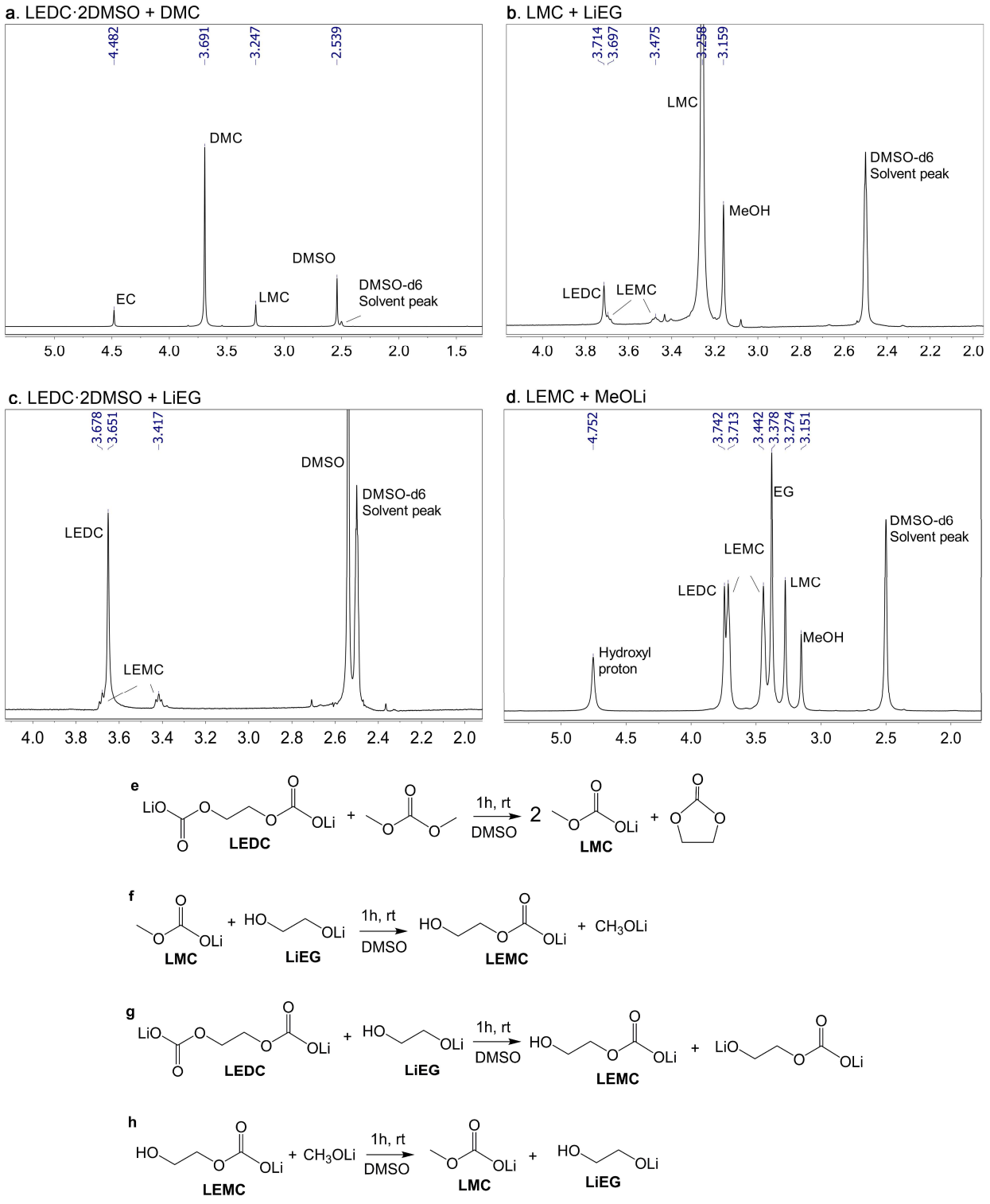


**Supplementary Figure 17.** $^{1}$H NMR spectra (500 MHz, 25 °C) of supernatant/solutions of reactions (a) LEDC + DMC, (b) LMC + LiEG, (c) LEDC + LiEG and (d) LEMC + MeOLi, with the corresponding chemical equations shown in (e), (f), (g) and (h), respectively. Experimental details are described in the section of Experimental Procedures in the Supplementary Information.

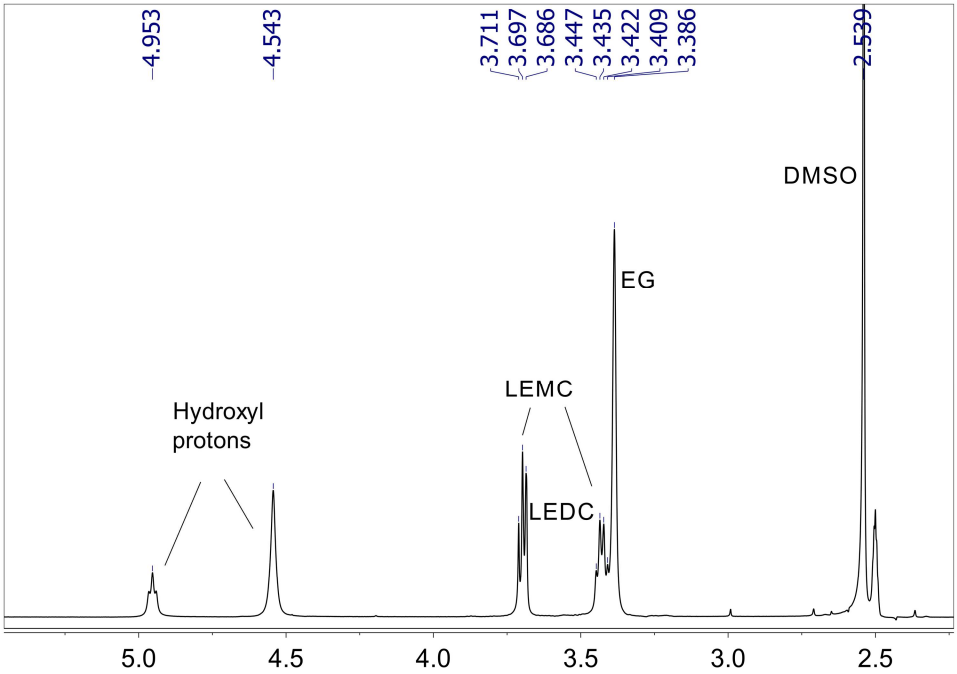


**Supplementary Figure 18.** $^{1}$H NMR spectrum (400 MHz, 25 °C) of the solution of reaction LEDC + EG in DMSO-$d_6$. As expected, adding EG to the solution of LEDC in DMSO-$d_6$ leads to the formation of LEMC. Experimental details are described in the section of Experimental Procedures in the Supplementary Information.

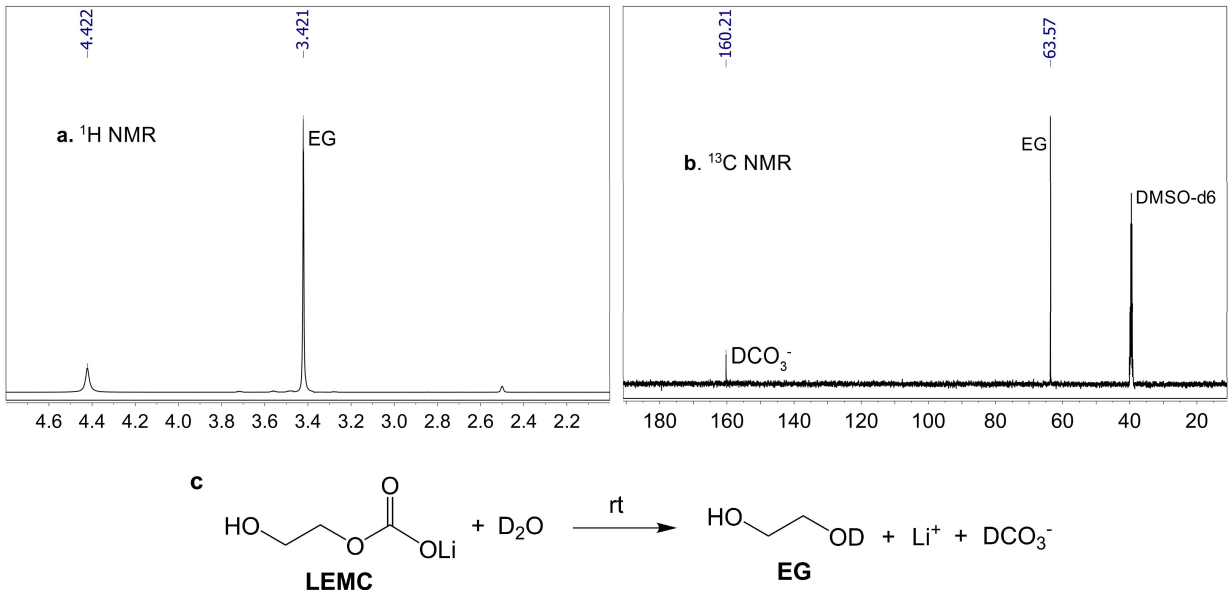


**Supplementary Figure 19.** (a) $^{1}$H NMR and (b) $^{13}$C {$^{1}$H} NMR spectra (500 MHz, 25 $^{o}$C) of LEMC (0.53 mol/L) in DMSO-$d_6$ when excess $D_2O$ is added. The addition of $D_2O$ hydrolyzes LEMC and LEDC, in generation of EG as the only organic species in the solution. (c) shows the corresponding chemical reaction.

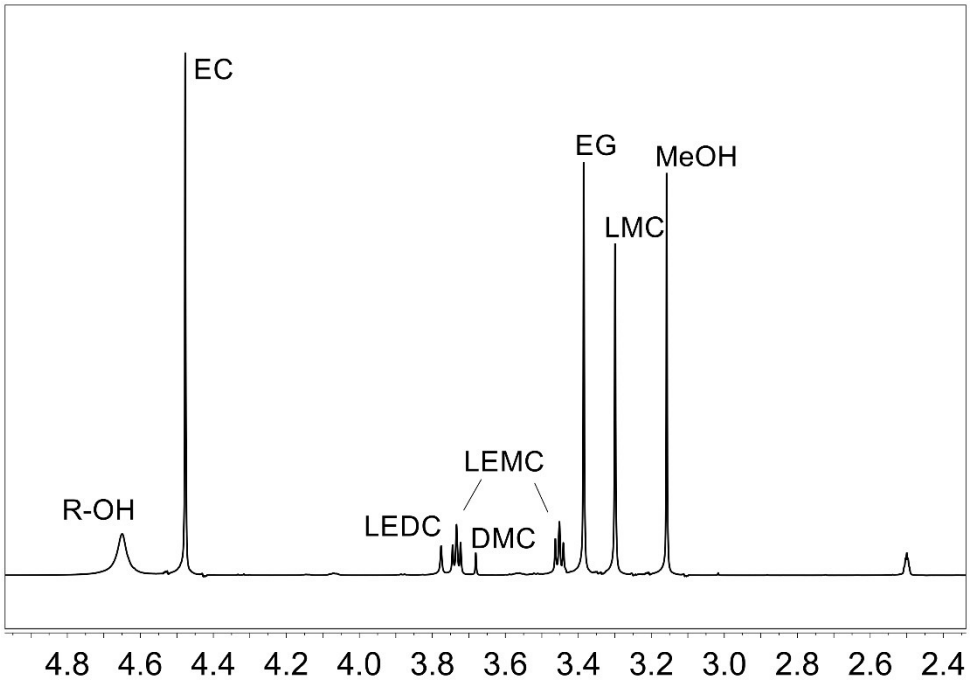


**Supplementary Figure 20**. $^{1}$H NMR spectra (DMSO-$d_6$, 500 MHz, 25 °C) of LEMC + DMC dissolved in DMSO-$d_6$. Initial concentration before equilibria: 22 mg DMC + 67 mg LEMC in 1 g DMSO-$d_6$. Dissolving LEMC and DMC together into DMSO-$d_6$ instantly results in multiple equilibria. The most important equilibria in the system have been documented in Fig. 4 e-f.

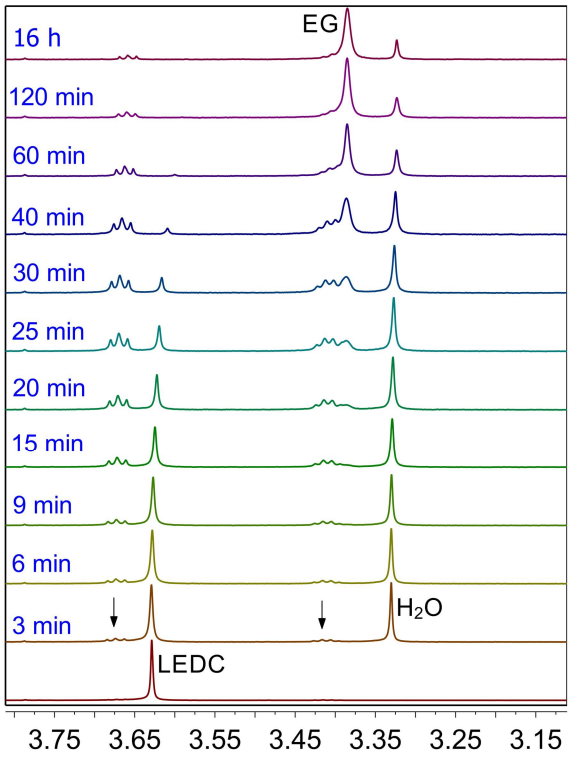


**Supplementary Figure 21**. $^{1}$H NMR (500 MHz, 25 °C, LEDC concentration: ~ 0.02 mol/L) of LEDC in DMSO-$d_6$ with $H_2O$ (~ 1.5 equiv.) added. Arrows indicate peaks of LEMC generated from hydrolysis of LEDC. The addition of the ~ 1.5 equiv. $H_2O$ to a DMSO-$d_6$ solution of LEDC leads to the hydrolysis of LEDC, giving measurable LEMC after 3 min. The LEDC is completely consumed after 60 min. but the subsequent LEMC hydrolysis to give EG is significantly slower such that residual LEMC remains after 16 h of reaction.

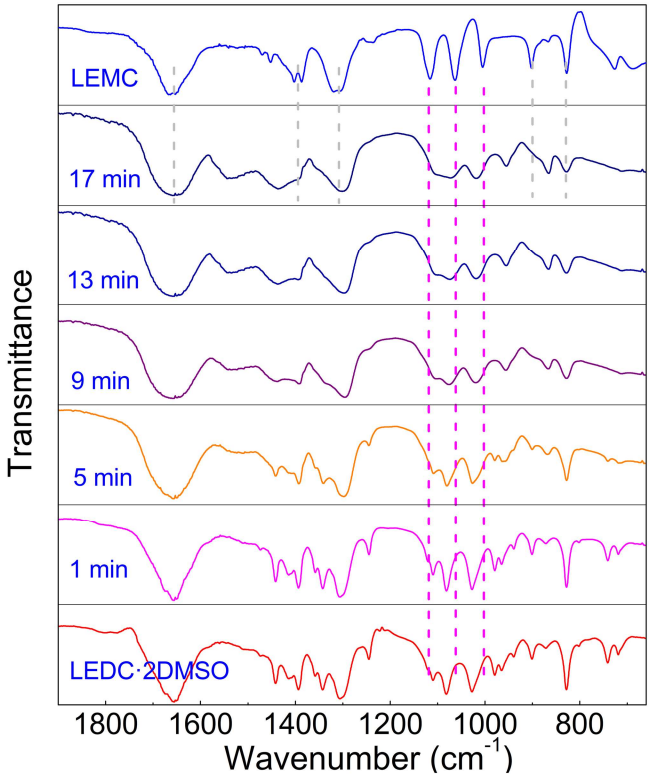


**Supplementary Figure 22**. FTIR (diffuse reflectance, DRIFTS) spectroscopy on hydrolysis of LEDC·2DMSO towards moisture (air, *ca.* 40% R.I.H.). The hydrolysis of LEDC towards moisture likely leads to the generation of LEMC. As indicated by the dashed magenta lines, after LEDC·2DMSO is exposed to air for 17 min, three new bands emerge at 1116, 1063 and 1005 $cm^{-1}$, which are suggestive of LEMC formation. The similarities in the IR spectral features of LEDC and LEMC, and the presence of DMSO solvates in the LEDC sample complicate the interpretation of the IR data, but the time dependent spectra show that the LEDC•2DMSO sample quickly decomposes in humid air and that LEMC is a likely by-product.

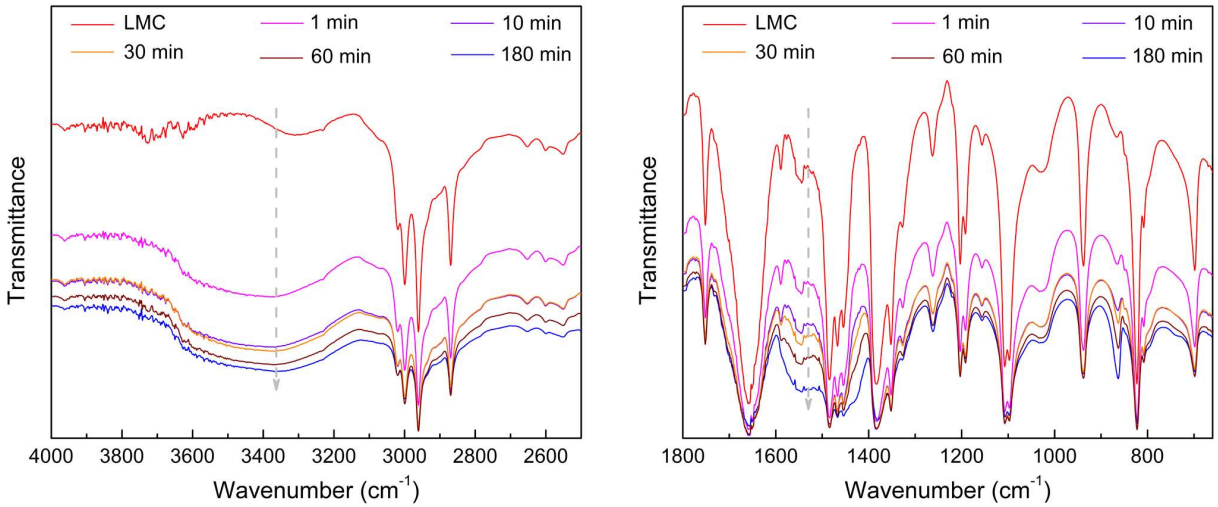


**Supplementary Figure 23**. FTIR (diffuse reflectance, DRIFTS) spectra of LMC when exposed to moisture (air, *ca.* 40% R.I.H.) for different amount of time. The broad "bump" peak in FTIR spectra at 3400 $cm^{-1}$ indicates absorption of moisture from air. Hydrolysis of LMC generates inorganic carbonate species ($HCO_3^-$), as is indicated by the formation of new broad bands at *ca.* 1520 $cm^{-1}$. LMC shows moderate stability with major patterns retained after an 1 h exposure.

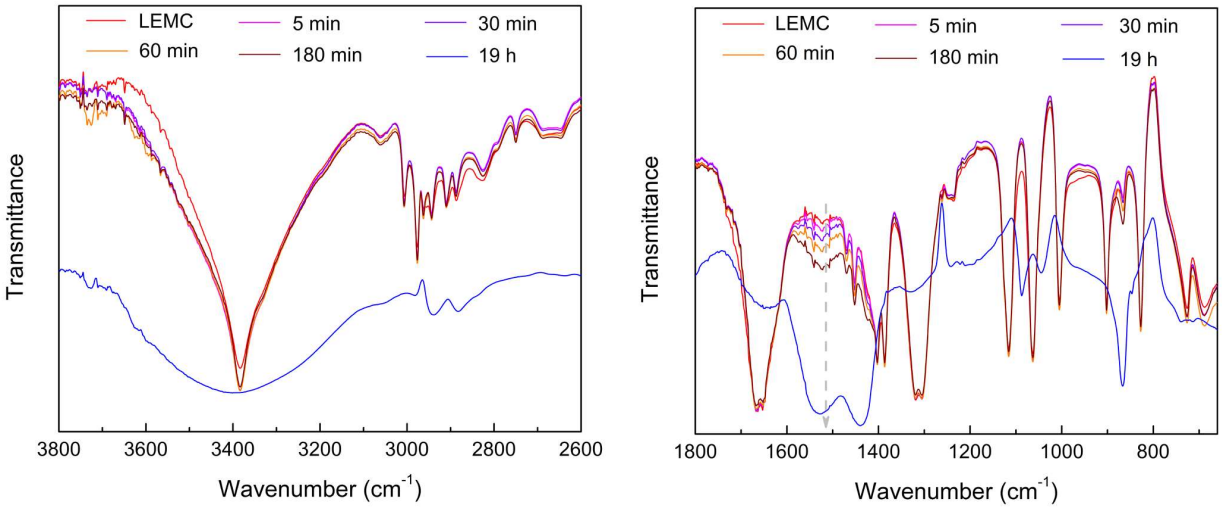


**Supplementary Figure 24**. FTIR (diffuse reflectance, DRIFTS) spectra of LEMC when exposed to moisture (air, *ca.* 40% R.I.H.) for different amount of time. The broad "bump" peak in FTIR spectra at 3400 $cm^{-1}$ indicates absorption of moisture from air. Hydrolysis of LEMC generates inorganic carbonate species ($HCO_3^-$), as is indicated by the formation of new broad bands at *ca.* 1500 $cm^{-1}$. LEMC showed the highest stability towards moisture, as no visible decompositions could be detected after a 3 h exposure.

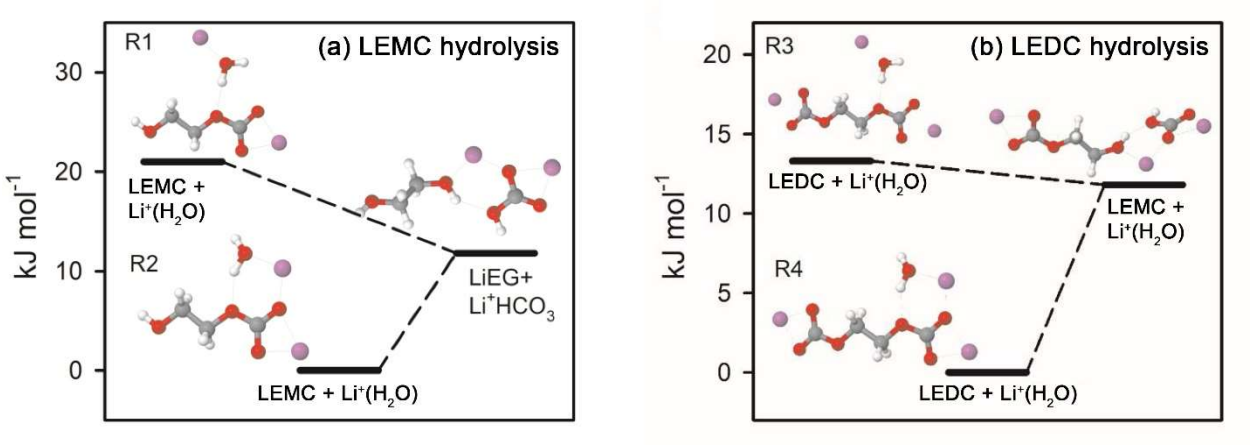


**Supplementary Figure 25**. Free energy of the (a) LEMC and (b) LEDC hydrolysis reactions from G4MP2 calculations with reactants and products surrounded by a polarized continuum model PCM (dielectric constant e=20). See *Experimental Procedures* for calculation details.

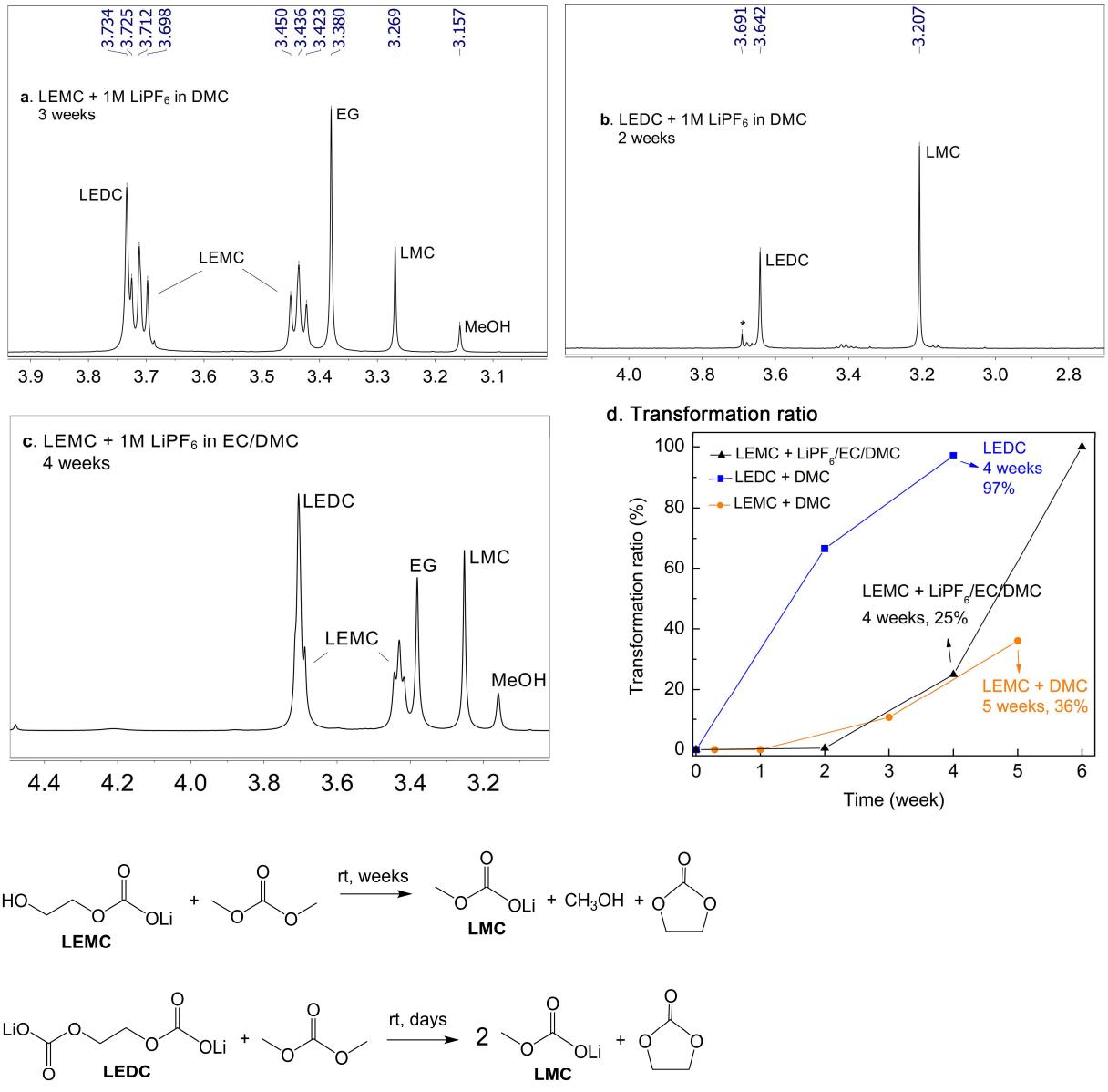





**Supplementary Figure 26.** $^1$H NMR spectra (DMSO-$d_6$, 500 MHz, 25 °C) of the precipitates from reactions (a) LEMC + DMC, (b) LEDC + DMC and (c) LEMC + 1M $LiPF_6$ in EC/DMC, with the corresponding chemical equations shown in (e) and (f). No DMSO is added in the reactions. Figure (d) shows the ratios of transformation for the 3 reactions (black: LEMC + $LiPF_6$/EC/DMC, blue: LEDC + DMC, orange: LEMC + DMC) over different reaction times. The reactions occurring on liquid-solid interface are much more sluggish than when DMSO is used to solvate the reactants. After 5 weeks' reaction, the majority (74%) of LEMC was retained (orange). LEDC is likely more reactive, as the vast majority (97%) is already consumed after a 4 weeks' reaction (blue). Experimental details are described in the section of Experimental Procedures in the Supplementary Information.

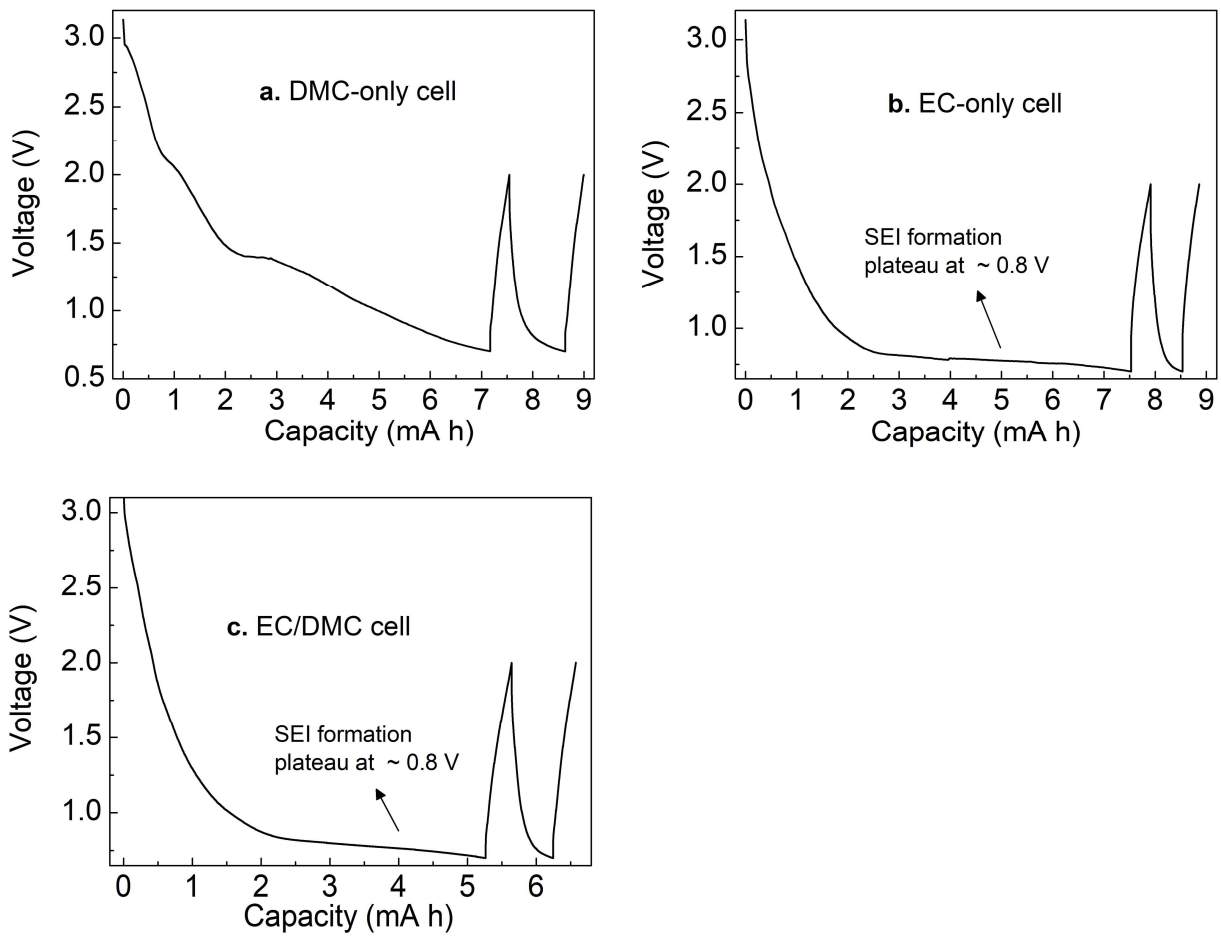


**Supplementary Figure 27**. 1st and 2nd cycles of a large graphite electrode (containing 400 mg graphite on a large Cu current collector) cycled from 0.7 – 2.0 V with Li foil as counter electrodes in different electrolytes (a) 1M $LiPF_6$ in DMC, (b) 1M $LiPF_6$ in EC and (c) 1M $LiPF_6$ in EC/DMC. The plateaus observed in (a) at *ca*. 2.1 V and 1.4 V are attributed to electrochemical reduction of $(Li^+)_x(PF_6^-)_y$ clusters in the DMC-only electrolyte solution.[39]

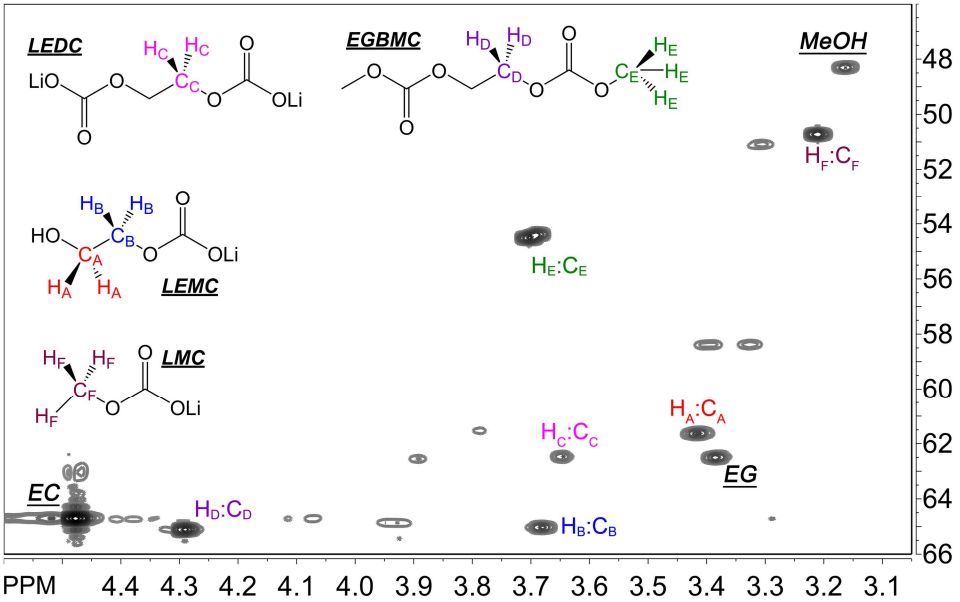


**Supplementary Figure 28**. $^{1}$H-$^{13}$C HSQC spectra (800 MHz, 25 °C) in DMSO-$d_6$ of graphite SEI layers grown in EC/DMC electrolyte.

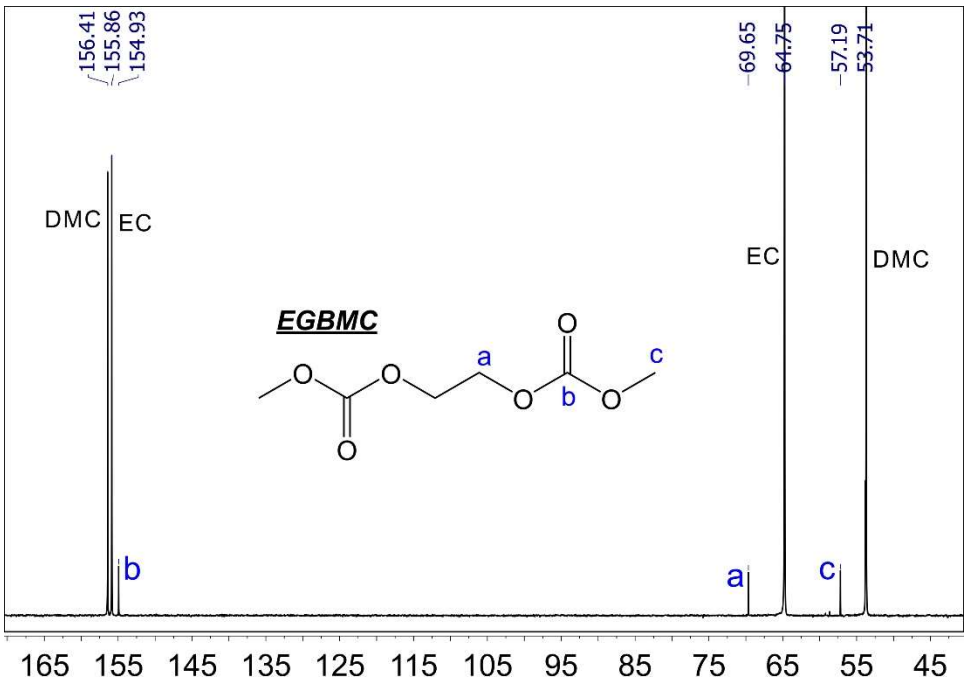


**Supplementary Figure 29.** $^{13}C$ {$^{1}H$} NMR spectra (126 MHz, 25 °C) on the electrolyte solution (*i.e.* 1M $LiPF_6$ in EC/DMC) after a graphite electrode is cycled. EGBMC is detected as a major new species in the electrolyte.

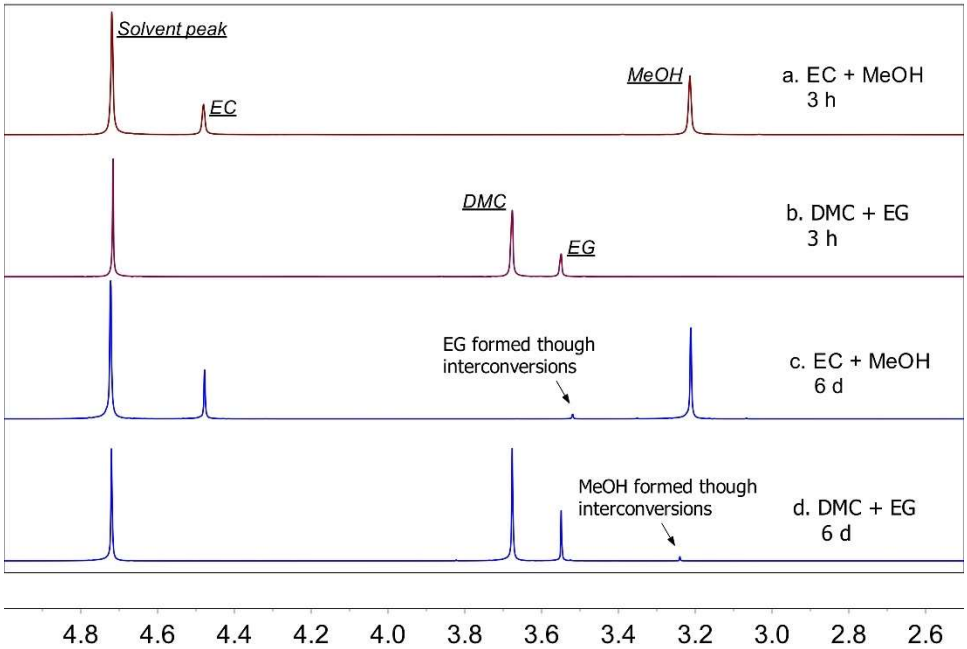


**Supplementary Figure 30**. $^{1}$H NMR spectra (500 MHz, 25 °C) when (a, c) EC (*ca.* 0.4 mol/L) + MeOH (*ca.* 1 mol/L) and (b, d) DMC (*ca.* 0.8 mol/L) + EG (*ca.* 0.2 mol/L) were dissolved in 1 g 0.1 M DCl/$D_2O$ aqueous solutions. NMR spectra were collected at (a, b) 3 h and (c, d) 6 days after mixing the components. In this acidic aqueous solution, the reactions between organic carbonates and alcohol are largely averted. No interconversions were detected within 3 h. After 6 days of mixing, only tiny amount of interconversion products (transformation ratio: *ca.* 2%) was detected.

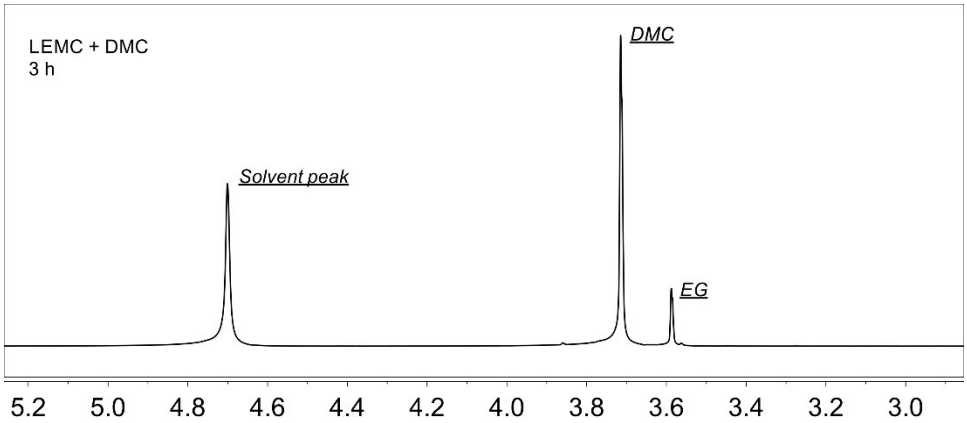


**Supplementary Figure 31**. $^{1}$H NMR spectra (500 MHz, 25 $^{o}$C) on solution of mixture of DMC (*ca.* 0.9 mol/L) and LEMC (*ca.* 0.1 mol) in 0.1 M DCl/$D_2O$ (1 g). No products from interconversion reactions were detected. This experiment indicated that upon hydrolysis in acidic aqueous solution, the interconversion reactions/equilibria between LEMC and DMC are averted.

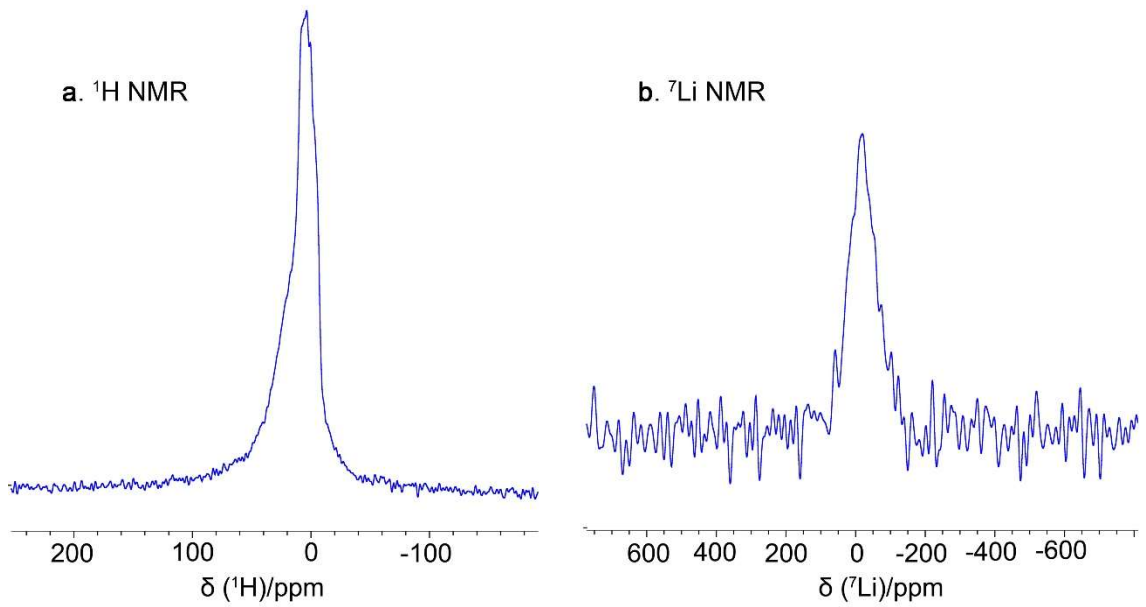


**Supplementary Figure 32**. 1D solid-state NMR spectra. (a) $^{1}H$ (850 MHz) and (b) $^{7}Li$ (330 MHz) one-pulse MAS NMR spectra of SEI layers coated graphite powders. Very broad peaks were observed, possibly due to paramagnetic impurities.

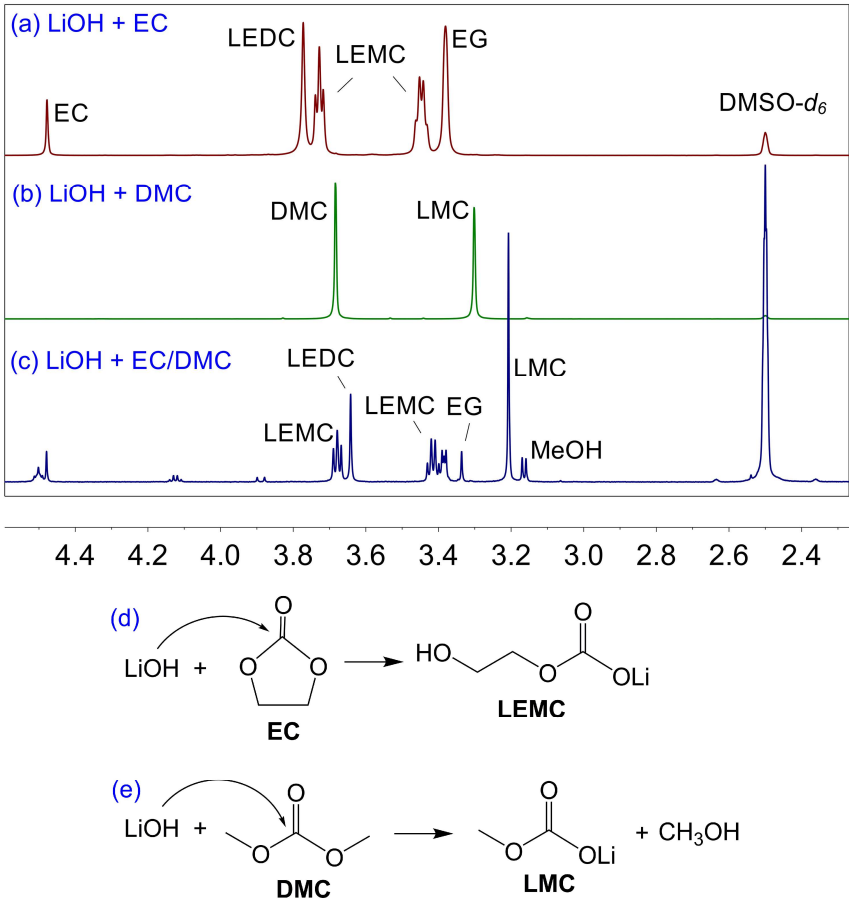


**Supplementary Figure 33**. (a) $^1$H NMR (DMSO-$d_6$, 500 MHz, 25 °C) of precipitates from reactions of anhydrous LiOH with (a) 1M $LiPF_6$/EC, (b) 1M $LiPF_6$/DMC and (c) 1M $LiPF_6$/EC/DMC. (See the experimental section in the supplementary information for details). Nucleophilic addition of LiOH to EC and DMC gives LEMC and LMC, respectively, according to the reaction equations in figure (d) and (e).

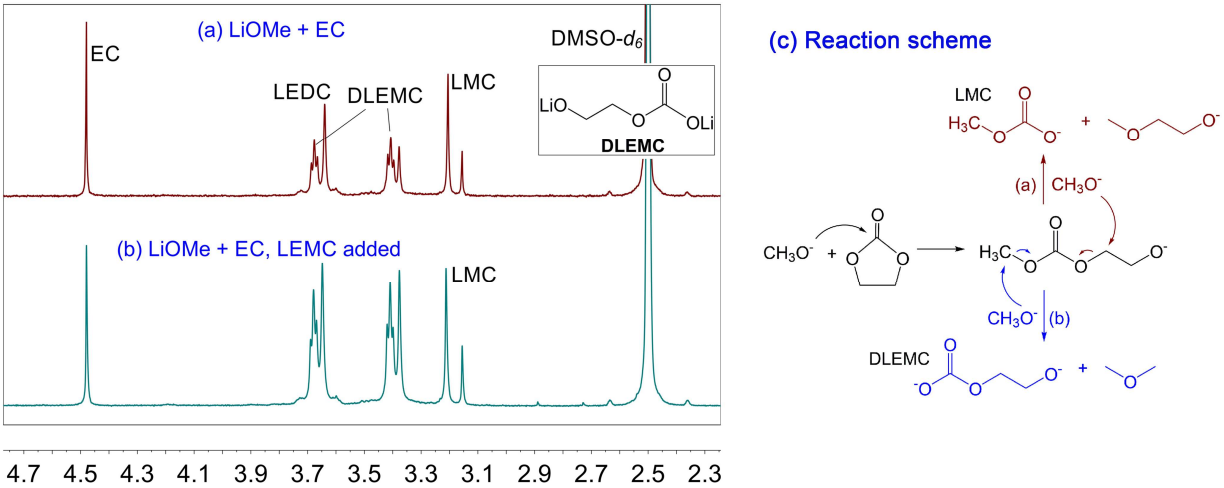


**Supplementary Figure 34**. (a) $^1$H NMR (DMSO-$d_6$, 600 MHz, 25 °C) of precipitates from reactions of MeOLi with EC at 50 °C (See the experimental section in the supplementary information for details). Synthesized LEMC is added into the NMR solution and the NMR spectrum is recollected to give (b). Peak intensities increase while no new peaks were observed in (b) compared with (a), indicating the products detected in (a) are di-lithiated ethylene mono-carbonate (DLEMC). (c) shows a scheme for proposed reaction mechanisms.

## 3. Supplementary Tables

**Supplementary Table 1**. FTIR spectra band assignments of LMC, LEMC and LEDC·2DMSO. [a]

| Band assignments | LEMC | LMC | LEDC·2DMSO |
|---|---|---|---|
| Hydrogen bonding O-H Stretching | 3383 (st) | | |
| C-H Stretching | 3006 (sm) | 3018 (sm) | 3018 (sm) |
| | 2976 (sm) | 2999 (sm) | 2998 (sm) |
| | 2944 (sm) | 2961 (sm) | 2982 (sm) |
| | 2909 (sm) | 2870 (sm) | 2966 (sm) |
| | 2887 (sm) | | 2924 (sm) |
| | 2827 (sm) | | 2908 (sm) |
| C=O Stretching | 1667 (st) | 1751 (med) | 1656 (st) |
| | 1664 (st) | 1659 (st) | 1652 (st) |
| | 1653 (st) | 1651 (st) | |
| | | 1589 (sm) | |
| C-H deformation | 1452 (sm) | 1485 (st) | 1442 (med) |
| | | 1467 (med) | |
| | | 1455 (med) | |
| CO3 asymmetric stretching | 1402 (st) | 1383 (st) | 1394 (st) |
| | 1387 (st) | 1352 (med) | 1342 (st) |
| CH2 Wagging | 1319 (st) | | 1306 (st) |
| C-O-C symmetric & asymmetric stretching | 1116 (st) | 1107 (st) | 1110 (med) |
| | | 1097 (st) | 1082 (st) |
| Alcohol C-O stretching | 1063 (st) | | |
| CO3 symmetric Stretching | 1005 (med) | 938 (med) | 1027 (st) |
| | 902 (med) | | |
| CO3 Bending | 828 (med) | 823 (st) | 828 (st) |
| O-C=O deformation | 726 (med) | 699 (med) | 741 (med) |
| | 688 (med) | | 719 (sm) |

[a] sm: small. med: medium. st: strong. sh: shoulder.

**Supplementary Table 2**. Selected bonding distances and angles of LEMC

| A | B | C | A-B-C / deg. | A-B / Å | B-C / Å |
|---|---|---|---|---|---|
| O1 | Li1 | O7 | 113.4 (4) | 1.917 (8) | 2.016 (9) |
| O1 | Li1 | O2 | 105.9 (4) | 1.917 (8) | 2.025 (9) |
| O1 | Li1 | O1 | 100.5 (4) | 1.917 (8) | 2.027 (9) |
| O1 | Li1 | O4 | 139.9 (4) | 1.917 (8) | 2.580 (9) |
| O7 | Li1 | O2 | 92.3 (4) | 2.016 (9) | 2.025 (9) |
| O7 | Li1 | O1 | 107.3 (4) | 2.016 (9) | 2.027 (9) |
| O7 | Li1 | O4 | 104.6 (3) | 2.016 (9) | 2.580 (9) |
| O2 | Li1 | O1 | 137.2 (5) | 2.025 (9) | 2.027 (9) |
| O2 | Li1 | O4 | 83.9 (3) | 2.025 (9) | 2.580 (9) |
| O1 | Li1 | O4 | 54.8 (2) | 2.027 (9) | 2.580 (9) |

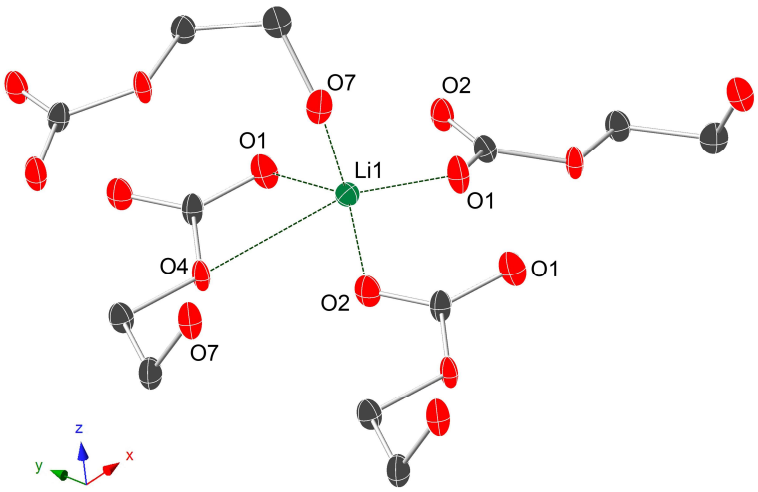

**Supplementary Table 3**. Selected bonding distances and angles of LMC

| A | B | C | A-B-C / deg. | A-B / Å | B-C / Å |
|---|---|---|---|---|---|
| O11A | Li1A | O12A | 113.3 (3) | 1.924 (6) | 1.954 (7) |
| O11A | Li1A | O22A | 117.2 (3) | 1.924 (6) | 1.956 (7) |
| O11A | Li1A | O21A | 89.9 (3) | 1.924 (6) | 1.976 (6) |
| O12A | Li1A | O22A | 112.1 (3) | 1.954 (7) | 1.956 (7) |
| O12A | Li1A | O21A | 108.1 (3) | 1.954 (7) | 1.976 (6) |
| O22A | Li1A | O21A | 114.3 (3) | 1.956 (7) | 1.976 (6) |

| A | B | C | A-B-C / deg. | A-B / Å | B-C / Å |
|---|---|---|---|---|---|
| O21A | Li2A | O12A | 116.0 (3) | 1.922 (6) | 1.946 (7) |
| O21A | Li2A | O22A | 114.8 (3) | 1.922 (6) | 1.988 (7) |
| O21A | Li2A | O11A | 88.9 (3) | 1.922 (6) | 2.011 (6) |
| O12A | Li2A | O22A | 110.3 (3) | 1.946 (7) | 1.988 (7) |
| O12A | Li2A | O11A | 112.0 (3) | 1.946 (7) | 2.011 (6) |
| O22A | Li2A | O11A | 113.4 (3) | 1.988 (7) | 2.011 (6) |

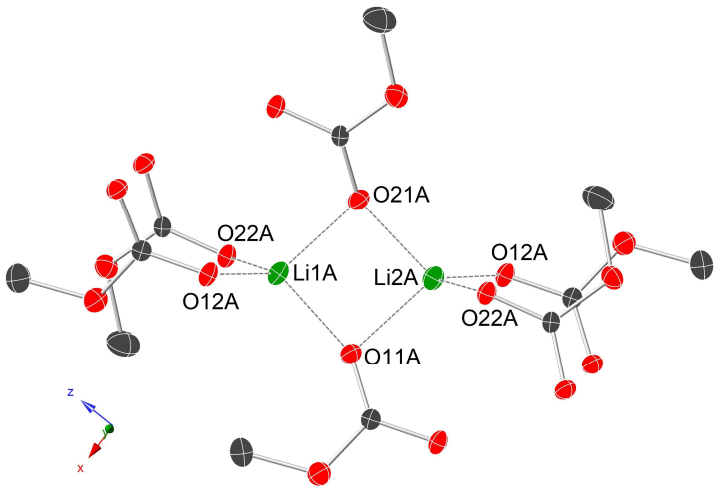

**Supplementary Table 4**: Comparison of experimental and GIPAW calculated chemical shifts (in ppm) for LEMC.

| Atom | $\delta_{calc}$ /ppm | $\delta_{exp}$/ppm |
|---|---|---|
| H 3 | 5.0 | 5.1 |
| H 2 | 3.5 | 3.4 |
| H 3 | 3.1 | |
| H 4 | 3.6 | |
| H 5 | 3.0 | |
| C 1 | 67.2 | |
| C 2 | 58.5 | |
| C 3 | 159.2 | |
| Li 1 | 1.2 | 1.1 |

**Supplementary Table 5**: Comparison of experimental and GIPAW calcualted[a] chemical shifts (in ppm) for LMC.

| Atom | $\delta_{calc}$ /ppm (structure 1)[b] | $\delta_{calc}$ /ppm (structure 2)[c] | $\delta_{exp}$/ppm |
|---|---|---|---|
| H 1, H2, H3 | 3.6 | 3.7 | 3.4 |
| H 4, H 5, H6 | 3.5 | 3.5 | |
| H 7, H 8, H 9 | 3.7 | 3.7 | 3.1 |
| H 10, H 11, H 12 | 3.5 | 3.5 | |
| C 1 | 160.5 | 160.5 | |
| C 2 | 52.9 | 53.0 | |
| C 3 | 160.7 | 160.8 | |
| C 4 | 55.0 | 54.9 | |
| C 5 | 160.6 | 160.4 | |
| C 6 | 52.9 | 53.0 | |
| C 7 | 160.8 | 160.8 | |
| C 8 | 54.9 | 54.9 | |
| Li 1 | 0.6 | 0.5 | 0.5 |
| Li 2 | 0.4 | 0.3 | |
| Li 3 | 0.6 | 0.5 | |
| Li 4 | 0.4 | 0.4 | |

[a]Calculated isotropic $^{1}H$ chemical shifts for the $CH_3$ groups correspond to an average for the three protons.

[b,c]Structure 1 and structure 2 correspond to the two motifs in the disordered layer of LMC crystal structure.

# 4. References


1 Kocak, F. S. *et al.* Surprising Acid/Base and Ion-Sequestration Chemistry of Sn94–: HSn93–, Ni@ HSn93–, and the Sn93–Ion Revisited. *J. Am. Chem. Soc.* **134**, 9733-9740 (2012).

2 Brown, S. P. Probing proton–proton proximities in the solid state. *Prog. Nucl. Magn. Reson. Spectrosc.* **4**, 199-251 (2007).

3 Sommer, W., Gottwald, J., Demco, D. & Spiess, H. W. Dipolar heteronuclear multiple-quantum NMR spectroscopy in rotating solids. *J. Magn. Reson., Ser A* **113**, 131-134 (1995).

4 Schnell, I., Lupulescu, A., Hafner, S., Demco, D. E. & Spiess, H. W. Resolution enhancement in multiple-quantum MAS NMR spectroscopy. *J. Magn. Reson.* **133**, 61-69 (1998).

5 Oas, T., Griffin, R. & Levitt, M. Rotary resonance recoupling of dipolar interactions in solid‐state nuclear magnetic resonance spectroscopy. *J. Chem. Phys.* **89**, 692-695 (1988).

6 Gan, Z., Amoureux, J. P. & Trébosc, J. Proton-detected 14N MAS NMR using homonuclear decoupled rotary resonance. *Chem. Phys. Lett.* **435**, 163-169 (2007).

7 Webber, A. L. *et al.* Identifying guanosine self assembly at natural isotopic abundance by high-resolution 1H and 13C solid-state NMR spectroscopy. *J. Am. Chem. Soc.* **133**, 19777-19795 (2011).

8 Costa, P., Gross, J., Hong, M. & Griffin, R. Solid-state NMR measurement of ψ in peptides: a NCCN 2Q-heteronuclear local field experiment. *Chem. Phys. Lett.* **280**, 95-103 (1997).

9 Morcombe, C. R. & Zilm, K. W. Chemical shift referencing in MAS solid state NMR. *J. Magn. Reson.* **162**, 479-486 (2003).

10 Liang, Y. *et al.* A Clathrate‐I Phase with Li–Ge Framework. *Chem. Eur. J.* **18**, 9818-9822 (2012).

11 Pöppler, A.-C., Walker, D. & Brown, S. P. A combined NMR crystallographic and PXRD investigation of the structure-directing role of water molecules in orotic acid and its lithium and magnesium salts. *CrystEngComm* **19**, 224-236 (2017).

12 Clark, S. J. *et al.* First principles methods using CASTEP. *Zeitschrift für Kristallographie-Crystalline Materials* **220**, 567-570 (2005).

13 Segall, M. *et al.* First-principles simulation: ideas, illustrations and the CASTEP code. *J. Phys.: Condens. Matter* **14**, 2717 (2002).

14 Pickard, C. J. & Mauri, F. All-electron magnetic response with pseudopotentials: NMR chemical shifts. *Phys. Rev. B* **63**, 245101 (2001).

15 Perdew, J. P., Burke, K. & Ernzerhof, M. Generalized gradient approximation made simple. *Phys. Rev. Lett.* **77**, 3865 (1996).

16 Yates, J. R., Pickard, C. J. & Mauri, F. Calculation of NMR chemical shifts for extended systems using ultrasoft pseudopotentials. *Phys. Rev. B* **76**, 024401 (2007).

17 Monkhorst, H. J. & Pack, J. D. Special points for Brillouin-zone integrations. *Phys. Rev. B* **13**, 5188 (1976).

18 Harris, R. K., Hodgkinson, P., Pickard, C. J., Yates, J. R. & Zorin, V. Chemical shift computations on a crystallographic basis: some reflections and comments. *Magn. Reson. Chem.* **45**, S174-S186 (2007).

19 Reddy, G. M. *et al.* An NMR crystallography study of the hemihydrate of 2′, 3′-O-isopropylidineguanosine. *Solid State Nucl. Magn. Reson.* **65**, 41-48 (2015).

20 Sturniolo, S. *et al.* Visualization and processing of computed solid-state NMR parameters: MagresView and MagresPython. *Solid State Nucl. Magn. Reson.* **78**, 64-70 (2016).

21 Frisch, M. *et al.* (Rev, 2016).

22 Mayhall, N. J., Raghavachari, K., Redfern, P. C. & Curtiss, L. A. Investigation of Gaussian4 theory for transition metal thermochemistry. *J. Phys. Chem. A* **113**, 5170-5175 (2009).
23 Curtiss, L. A., Redfern, P. C. & Raghavachari, K. Gn theory. *Wiley Interdisciplinary Reviews: Computational Molecular Science* **1**, 810-825 (2011).
24 Shi, S. Q. *et al.* Direct Calculation of Li-Ion Transport in the Solid Electrolyte Interphase. *J. Am. Chem. Soc.* **134**, 15476-15487, doi:10.1021/ja305366r (2012).
25 Shi, S. Q., Qi, Y., Li, H. & Hector, L. G. Defect Thermodynamics and Diffusion Mechanisms in Li2CO3 and Implications for the Solid Electrolyte Interphase in Li-Ion Batteries. *J. Phys. Chem. C* **117**, 8579-8593 (2013).
26 Dawson, J. A. *et al.* Elucidating lithium-ion and proton dynamics in anti-perovskite solid electrolytes. *Ener. & Env. Sci.*, doi:10.1039/C8EE00779A (2018).
27 Howard, J., Hood, Z. D. & Holzwarth, N. A. W. Fundamental aspects of the structural and electrolyte properties of $Li_2OHCl$ from simulations and experiment. *Phys. Rev. Mater.* **1**, 075406 (2017).
28 Song, A. Y. *et al.* Protons Enhance Conductivities in Lithium Halide Hydroxide/Lithium Oxyhalide Solid Electrolytes by Forming Rotating Hydroxy Groups. *Adv. Energy Mater.* **8**, 1700971 (2018).
29 He, X., Zhu, Y. & Mo, Y. Origin of fast ion diffusion in super-ionic conductors. *Nature communications* **8**, 15893 (2017).
30 Lippert, G., Hutter, J. & Parrinello, M. A hybrid Gaussian and plane wave density functional scheme. *Mol. Phys.* **92**, 477-487 (1997).
31 VandeVondele, J. *et al.* QUICKSTEP: Fast and accurate density functional calculations using a mixed Gaussian and plane waves approach. *Comput. Phys. Comm.* **167**, 103-128 (2005).
32 Goedecker, S., Teter, M. & Hutter, J. Separable dual-space Gaussian pseudopotentials. *Phys. Rev. B* **54**, 1703-1710 (1996).
33 Hartwigsen, C., Goedecker, S. & Hutter, J. Relativistic separable dual-space Gaussian pseudopotentials from H to Rn. *Phys. Rev. B* **58**, 3641-3662 (1998).
34 Grimme, S., Antony, J., Ehrlich, S. & Krieg, H. A consistent and accurate ab initio parametrization of density functional dispersion correction (DFT-D) for the 94 elements H-Pu. *J. Chem. Phys.* **132** (2010).
35 Perdew, J. P., Burke, K. & Ernzerhof, M. Generalized gradient approximation made simple. *Phys. Rev. Lett.* **77**, 3865-3868 (1996).
36 Weber, V., VandeVondele, J., Hutter, J. & Niklasson, A. M. N. Direct energy functional minimization under orthogonality constraints. *J. Chem. Phys.* **128** (2008).
37 Bussi, G., Donadio, D. & Parrinello, M. Canonical sampling through velocity rescaling. *J. Chem. Phys.* **126** (2007).
38 Xu, K. *et al.* Syntheses and characterization of lithium alkyl mono-and dicarbonates as components of surface films in Li-ion batteries. *J. Phys. Chem. B* **110**, 7708-7719 (2006).
39 Borodin, O. Challenges with Prediction of Battery Electrolyte Electrochemical Stability Window and Guiding the Electrode–Electrolyte Stabilization. *Current Opinion in Electrochemistry* (2018).